Available online at www.sciencedirect.com

ScienceDirect

Geochimica et Cosmochimica Acta 172 (2016) 159–176

Geochimica et Cosmochimica Acta

www.elsevier.com/locate/gca

Precise oxygen and hydrogen isotope determination in nanoliter quantities of speleothem inclusion water by cavity ring-down spectroscopic techniques

Ryu Uemura [a,*], Masashi Nakamoto [a], Ryuji Asami [b], Satoru Mishima [a], Masakazu Gibo [a], Kosuke Masaka [a], Chen Jin-Ping [c], Chung-Che Wu [c], Yu-Wei Chang [c], Chuan-Chou Shen [c,*]

[a] *Department of Chemistry, Biology, and Marine Science, Faculty of Science, University of the Ryukyus, 1 Senbaru, Nishihara, Okinawa 903-0213, Japan*

[b] *Department of Earth Science, Faculty of Science, University of the Ryukyus, 1 Senbaru, Nishihara, Okinawa 903-0213, Japan*

[c] *High-Precision Mass Spectrometry and Environment Change Laboratory (HISPEC), Department of Geosciences, National Taiwan University, Taipei 10617, Taiwan, ROC*

Received 12 September 2014; accepted in revised form 18 September 2015; Available online 30 September 2015

Abstract

Speleothem inclusion-water isotope compositions are a promising new climatic proxy, but their applicability is limited by their low content in water and by analytical challenges. We have developed a precise and accurate isotopic technique that is based on cavity ring-down spectroscopy (CRDS). This method features a newly developed crushing apparatus, a refined sample extraction line, careful evaluation of the water/carbonate adsorption effect. After crushing chipped speleothem in a newly-developed crushing device, released inclusion water is purified and mixed with a limited amount of nitrogen gas in the extraction line for CRDS measurement. We have measured 50–260 nL of inclusion water from 77 to 286 mg of stalagmite deposits sampled from Gyokusen Cave, Okinawa Island, Japan. The small sample size requirement demonstrates that our analytical technique can offer high-resolution inclusion water-based paleoclimate reconstructions. The 1σ reproducibility for different stalagmites ranges from ±0.05 to 0.61‰ for $\delta^{18}O$ and ±0.0 to 2.9‰ for δD. The δD vs. $\delta^{18}O$ plot for inclusion water from modern stalagmites is consistent with the local meteoric water line. The 1000 ln α values based on calcite and fluid inclusion measurements from decades-old stalagmites are in agreement with the data from present-day farmed calcite experiment. Combination of coeval carbonate and fluid inclusion data suggests that past temperatures at 9–10 thousand years ago (ka) and 26 ka were 3.4 ± 0.7 °C and 8.2 ± 2.4 °C colder than at present, respectively.

1. INTRODUCTION

Owing to their abundant tracer composition, as well as their absolute chronology and applicability from the Anthropocene to the Pleistocene, speleothems are considered one of the most important natural archives of past climate (Fairchild et al., 2006; Fairchild and Baker, 2012). The speleothem carbonate oxygen isotope ratio ($\delta^{18}O$) has been used as a proxy for precipitation (e.g., Wang et al., 2001, 2006, 2008; Bar-Matthews et al., 2003; Partin et al., 2007; Cheng et al., 2012; Ayliffe et al., 2013; Liu et al., 2014) or temperature (e.g., Gascoyne, 1992; Talma and Vogel, 1992; Dorale et al., 1998; Lauritzen and Lundberg,

* Corresponding authors. Tel.: +81 98 895 8526 (R. Uemura), +886 2 3366 5878 (C.-C. Shen).

E-mail addresses: ruemura@sci.u-ryukyu.ac.jp (R. Uemura), river@ntu.edu.tw (C.-C. Shen).

http://dx.doi.org/10.1016/j.gca.2015.09.017

0016-7037/

1999; Mangini et al., 2005; Sundqvist et al., 2013). However, the complex oxygen fractionation processes from the moisture source to the formation of speleothem hinder the quantitative reconstruction of past thermal and hydrological conditions (e.g., McDermott, 2004; Fairchild et al., 2006; Lachniet, 2009). The oxygen and hydrogen isotopic signatures of speleothem inclusion water in sealed cavities can offer a possibility of paleo temperature estimates and provide direct evidence of past hydrological cycles (e.g., McDermott, 2004).

Drip water can be trapped as fluid inclusions in defect intercrystalline spaces during crystallization, and these fluid inclusions constitute 0.01–0.5% of speleothem by weight (Schwarcz et al., 1976; McDermott et al., 2005). Recent studies have indicated that the isotopic compositions of inclusion water can match those of cave drip water (Dennis et al., 2001; Genty et al., 2002; Fleitmann et al., 2003; Demeny and Siklosy, 2008; van Breukelen et al., 2008; Zhang et al., 2008; Dublyansky and Spotl, 2009; Griffiths et al., 2010, 2013; Labuhn et al., 2015), suggesting that inclusion water may preserve the original isotopic features of paleo-rainwater. The first attempt at hydroclimatic application was conducted by Schwarcz et al. (1976). Related subsequent studies have been summarized by McDermott (2004) and McDermott et al. (2005). For example, Matthews et al. (2000) used the inclusion water hydrogen stable isotope ratio (δD) to reveal climate-driven changes in the Mediterranean meteoric water cycle over the past 120 thousand years (ka). Fleitmann et al. (2003) used inclusion water δD to clarify different glacial-interglacial moisture sources in Oman. Griffiths et al. (2010) used speleothem inclusion water $\delta^{18}O$ and coeval carbonate $\delta^{18}O$ data to reconstruct cave temperature and rainfall sequences over the past 12.64 ka in southern Indonesia.

Although the importance of speleothem fluid inclusion was recognized in the 1970s (Schwarcz et al., 1976), limitations in the volume of water and the analytical difficulties associated with isotopic measurements hindered subsequent studies. For example, in early labor-intensive studies, water was extracted using a vacuum line and converted to H_2 and/or equilibrated with CO_2 (Schwarcz et al., 1976; Harmon et al., 1979; Dennis et al., 2001) for isotope ratio mass spectrometric (IRMS) measurements. Continuous-flow mass spectrometry combined with pyrolysis at 1400 °C reduced the sample requirement to 0.1–0.2 μL of inclusion water and the measurement time (Vonhof et al., 2006; Dublyansky and Spotl, 2009). However, water still needs be converted to measurable gases, such as H_2 and CO.

The molecular conversion step can be avoided by using cavity ring-down spectroscopy (CRDS), a recently developed technique with low instrumental and running costs compared with IRMS methods (e.g., Brand et al., 2009; Gupta et al., 2009). In CRDS, an infrared laser is used to detect the isotopologues of water molecules, enabling the direct measurement of water $\delta^{18}O$ and δD. Newly developed CRDS techniques (Arienzo et al., 2013; Affolter et al., 2014) or other laser-based spectroscopy techniques (Czuppon et al., 2014) offer a 1σ reproducibility of ±0.4–0.5‰ for $\delta^{18}O$ and ±1.5–2.0‰ for δD for 0.4–1.2 μL of inclusion water. However, the requirement for a relatively large volume of inclusion water has hindered the development of a high-temporal-resolution speleothem hydroclimatic record.

In this study, we developed techniques for measuring the $\delta^{18}O$ and δD values of speleothem fluid inclusions with a water requirement of only hundreds of nanoliters (nL) by using CRDS methods. This paper describes the new analytical system and techniques in Section 2, their performance evaluation in Section 3.1, and the application of the results to paleoclimate reconstruction in Section 3.2.

2. EXPERIMENTS

2.1. Apparatus for measuring stable isotopes in inclusion water

2.1.1. Extraction and preparation device

Our experimental apparatus for water inclusion isotope measurements incorporates a crushing device made of glass and is illustrated schematically in Fig. 1. The apparatus is composed of the following: (1) a device to extract water from carbonate, (2) a dilution apparatus for on-line isotopic measurement, and (3) a CRDS unit. Carbonate was mechanically crushed in a vacuum, and the released water was cryogenically trapped using processes modified from Dennis et al. (2001). The dilution component is an adaptation of a commercially available liquid water evaporator (Picarro Inc. Santa Clara, California, USA) (Gupta et al., 2009).

The apparatus is constructed using custom-made parts connected with valves and tube fittings. Valves 1 and 2 are bellow-sealed valves (SS-4H, Swagelok Co., Solon, Ohio, USA). Pressure is monitored using a compact Pirani gauge (TPR280, Pfeiffer Vacuum, Asslar, Germany). Valve 3 is a two-way normally closed solenoid valve (A2016, Gems Sensors & Controls, Plainville, Connecticut, USA) with a timer relay (LT4H, Panasonic Corp., Osaka, Japan) that controls the amount of N_2 gas (99.99%) for dilution. Valve 4 is a three-way solenoid valve (A3314, Gems Sensors & Controls, Plainville, Connecticut, USA). A flow control valve (SS-SS1, Swagelok Co., Solon, Ohio, USA) is used to adjust the flow of H_2O to the CRDS. During isotope measurement, a mixture of water vapor and N_2 gas is bled through the flow control valve to the CRDS ('measure' position in Fig. 1). Between measurements, N_2 gas is supplied via Valve 4 ('purge' position in Fig. 1) to purge the CRDS. Gas flow in the CRDS is generated using a diaphragm pump (Pump 1; DAU-20, ULVAC, Miyazaki, Japan). The line is evacuated using an oil-sealed rotary vacuum pump (Pump 2; GLD-201B, ULVAC, Miyazaki, Japan) between measurements, and a cryogenic trap (1/4 inch o.d. stainless steel coil immersed in liquid N_2) is placed before the pump to speed up evacuation.

Three custom-designed devices are used to lower water adsorption: a crushing device, a trap/expansion-chamber, and an injection port.

The crushing device, which has an internal volume of 5 cm^3 and a surface area of 20 cm^2, is composed of Pyrex glass (a in Fig. 1). This device is a modified vacuum valve,

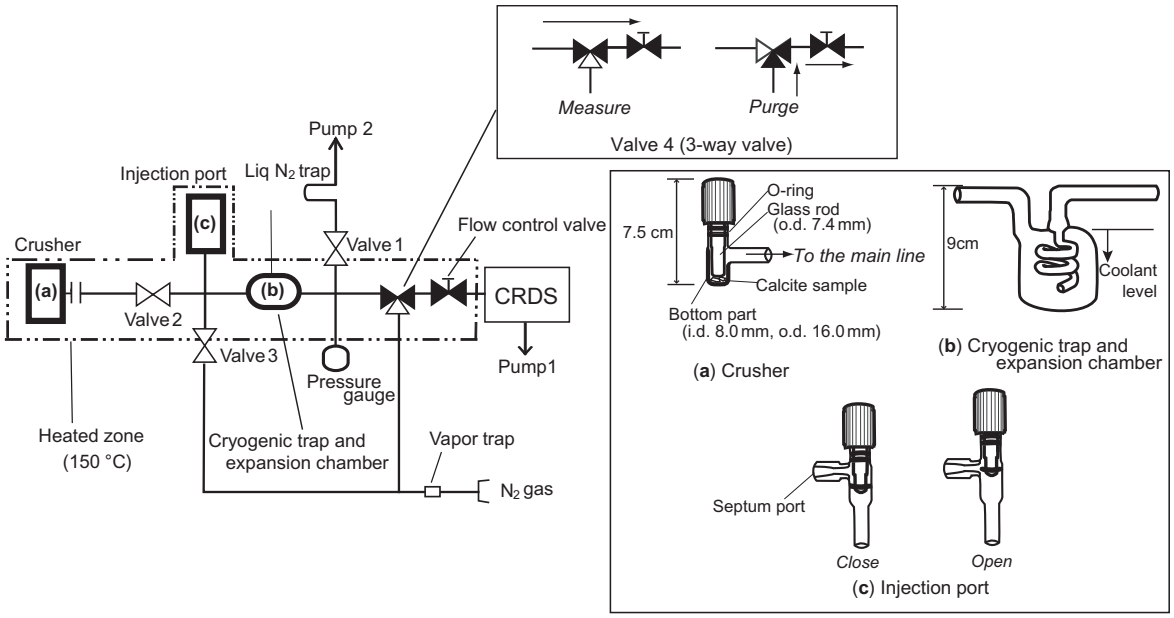

Fig. 1. Schematic diagram of the experimental apparatus. The chain line indicates components heated at 150 °C. An enclosed view of the custom-made devices is shown in the box on the right. (a) Speleothem crushing device; speleothem samples are placed onto the bottom of the device and then crushed by stroking the glass rod. (b) The two-in-one chamber is used as a cryogenic trap and expansion chamber. (c) Reference water injection port. The dimensions of the entire preparation line are 30 cm × 60 cm × 15 cm. Two positions of the 3-way valve are shown in the top box.

and the moving part is tightly sealed with two Viton O-rings (Koshin Rikagaku Co., Ltd., Tokyo, Japan). Stalagmite chips placed in the bottom of the crusher can be easily crushed by pressing the glass rod onto the sample by rotating the grip at the top of the threaded valve stem. All tested stalagmites, even crystalline hard samples, could be crushed using this Pyrex piston. For minerals harder than calcite (e.g., quartz), the glass crusher should be replaced with a stainless steel crusher. Compared with the stainless steel device, the glass crusher is easy to open and to clean its inside. The device is connected with a 3/8-inch Ultra-Torr adaptor (Swagelok Co., Solon, Ohio, USA), welded to a 1/4-inch VCR fitting (Swagelok Co., Solon, Ohio, USA). A 0.3-μm mesh gasket-type filter (Pureron Japan Co., Ltd., Fukushima, Japan) is installed in the face seal fitting to prevent contamination of the line by crushed calcite particles.

A cryogenic trap/expansion chamber (b in Fig. 1) made of Pyrex glass is used to collect the released water vapor. This chamber is a modification of a cryogenic trap for atmospheric vapor collection (Uemura et al., 2008). The internal spiral prevents the outflow of trapped ice and functions as an expansion volume chamber for mixing vapor with N_2 gas. To measure nanoliter samples, an internal volume of 50 cm^3 is used, which is only one third of the volume used in commercial vaporizers (Gupta et al., 2009).

The septum injection port (c in Fig. 1) is used to introduce liquid samples. A septum port is directly connected to a branched glass tube of a Pyrex glass vacuum valve (SDL valve, Koshin Rikagaku Co., Ltd., Tokyo, Japan). The device is connected with a 3/8-inch Ultra-Torr adaptor. Reference liquid water is injected using a plunger-in-needle syringe (0.5BR-7, SGE Inc., Victoria, Australia). The valve can be set to the 'close' position to stop leaking from the septum port.

To prevent water adsorption (Dennis et al., 2001), the entire line except the valve handles is maintained at 150 °C using three silicone cable heaters (100 W, 4 m) wrapped with aluminum tape and regulated with three controllers for the crusher, the trap, and the remaining part of the line (chain-line frame in Fig. 1). The heater for the cryogenic trap should be checked regularly and replaced when damaged due to the large temperature difference between −196 °C and 150 °C. All heated parts, except the cryogenic trap, are covered with insulating material (melamine foam).

2.1.2. Detector for determining of stable water oxygen and hydrogen isotopes

The oxygen and hydrogen isotopic compositions were determined by measuring water molecule isotopologues using a CRDS (Picarro L2130-i) at the University of the Ryukyus. This device functioned as the analyzer of the experimental apparatus (Fig. 1). The vapor $\delta^{18}O$ and δD were measured simultaneously. The hydrogen and oxygen isotope ratios are reported using δ notation, where $\delta = R_{sample}/R_{std} - 1$ and R_{sample} and R_{std} denote the isotope ratios ($^2H/^1H$ and $^{18}O/^{16}O$) of the sample and reference material, respectively. $\delta^{18}O$ and δD data were obtained relative to Vienna Standard Mean Ocean Water (VSMOW) for the inclusion water, precipitation, and drip water samples and were normalized to the Standard Light Antarctic Precipitation (SLAP) values of $\equiv -55.5‰$ for $\delta^{18}O$ and $-428‰$ for δD.

2.2. Procedure for inclusion water analysis

Before beginning the inclusion water analysis procedure, Valves 1 and 2 were opened, Valve 3 was closed and Valve 4 was set at the 'purge' position. The CRDS was purged with N_2 gas until isotopic measurement. During measurement, the sample chamber was connected to the CRDS with Valve 4 switched to the 'measure' position, and the N_2 gas supply was stopped. The sample vapor mixed with a limited amount of N_2 gas was slowly drawn through the flow-control valve into the CRDS during acquisition using a diaphragm pump. The peak shape was adjusted by regulating the flow control valve. Once it was optimized, the valve setting was maintained.

Chipped stalagmite subsamples were dried in a vacuum at room temperature (24–26 °C) for 1 h before measurement. The dried subsamples were placed in a crushing device at 150 °C by opening the threaded valve stem while Valve 2 was closed. The subsamples remained in the crusher (a in Fig. 1) while Valves 1 and 2 were opened and Valve 3 was closed. Next, the crusher was evacuated for 30 min until the pressure was <0.5 Pa, and the subsamples were then crushed with Valve 2 open and Valves 1 and 3 closed.

After the released water was evaporated, the pressure stabilized within 2 min. The temperature of the trap chamber was maintained at 150 °C, except during the cryogenic trapping process. Heating of the trap chamber (b in Fig. 1) was stopped 10 s before immersion in liquid N_2 for 10 min to trap the water vapor. Next, the crusher and trap chamber were separated by closing Valve 2. Then, the trap-chamber temperature was increased to −75 °C using a dry-ice/ethanol slush to vaporize CO_2. After 5 min, the released gas was evacuated by opening Valve 1, and Valve 1 was closed after CO_2 was pumped out. The trapped water sample was evaporated and desorbed for 6 min at 150 °C by heating the trap chamber. Dry N_2 gas (99.99%) was introduced by opening Valve 3 for 0.010 s. The pressure in the dilution/trap chamber after the admission of N_2 was approximately 150,000–25,000 Pa. The pressure is near the lowest pressure which the Picarro software does not give a "low pressure" alarm during the data acquisition process. The cavity pressure of the CRDS was always maintained at 6665 Pa. The H_2O/N_2 mixture gas flow was introduced from the dilution chamber/trap into the CRDS analyzer using a pre-optimized flow control valve for an 8-min isotopic measurement by changing the position of Valve 4 ('measure' position in Fig. 1).

During this measurement, the dry N_2 gas supply was separated from the CRDS and the dilution chamber/trap line using Valves 3 and 4. The H_2O/N_2 gas mixture was drawn from the chamber through a flow-control valve using the diaphragm pump of the CRDS analyzer. After conducting measurements, Valve 4 was switched to the 'purge' position, and Valves 1 and 2 were opened to prepare the line for the next measurement cycle. The CRDS analyzer was purged with dry N_2 gas until the next H_2O/N_2 mixture was sent to the analyzer. Fifteen minutes after the purging step, the H_2O concentration was decreased to a background level of 2–4 ppm.

The procedure used for the water samples was similar to that used for the speleothem carbonate. Before introducing the water sample, the crushing part was evacuated by leaving Valves 1 and 2 open for 30 min. After Valve 1 was closed, the water sample (20–300 nL) was injected through the septum while Valve 2 was opened. After injection, the injection port valve was closed to stop leakage from the septum port. The subsequent cryogenic trapping process and the remaining steps were identical to those for the carbonate samples.

2.3. Working reference, data acquisition and calibration

For water isotope analysis, an instrumental memory blank may result from the residuum of previous samples (Gupta et al., 2009). A laboratory working water reference OK11, $\delta^{18}O = -5.05‰$ and $\delta D = -28.21‰$, was analyzed before and after each sample measurement. Because the isotopic composition of the selected working standard OK11 is comparable to that of local rainfall (Uemura et al., 2012), the absolute bias introduced by the memory effect can be reduced.

A full sequence of inclusion water measurements was composed of one working water reference (OK11), one stalagmite sample, and three OK11 references. An example of a typical result is illustrated in Fig. 2a. Similar to the commercial evaporation device (Gupta et al., 2009), the flat parts of the $\delta^{18}O$ and δD peaks (average of 120 s; $n = 140$) (Fig. 2b and c) were used to calculate the isotope ratios. The isotopic data for inclusion water were calibrated using the average of the three reference injections following the inclusion measurement because they were size matched to the sample. This method corrects for the CRDS isotope dependence of the mixing ratio (e.g., Brand et al., 2009; Gupta et al., 2009; Arienzo et al., 2013). The isotopic ratio of the sample against VSMOW ($\delta_{sa/VSMOW}$) can be obtained from the followings:

$$\delta_{sa/VSMOW} \cdot 10^{-3} + 1 = \frac{\delta_{sa/meas} \cdot 10^{-3} + 1}{\delta_{WS/meas} \cdot 10^{-3} + 1} (\delta_{WS/VSMOW} \cdot 10^{-3} + 1) \quad (1)$$

where $\delta_{sa/meas}$ and $\delta_{WS/meas}$ are the measured isotope ratios of the sample and the working reference standard, respectively. The latter data include the calculated average of the three reference water injections. $\delta_{WS/VSMOW}$ is the isotope ratio of the working water reference relative to VSMOW, which was pre-determined using the IRMS techniques (Uemura et al., 2007). The effects of the volume of water on $\delta_{sa/meas}$ and $\delta_{WS/meas}$ cancel out in this calculation. Before this correction, the measured isotope ratios must be corrected for the memory effect described in Section 2.4. All data in the tables and figures were corrected for sample-size effects, except those in Figs. 2 and 7.

The crushed stalagmite remained in the crushing device during the reference water measurements to cancel out possible isotope fractionation on the freshly crushed calcite surface. The tests described in Section 3.1.3 demonstrated that this protocol produced negligible fractionation of

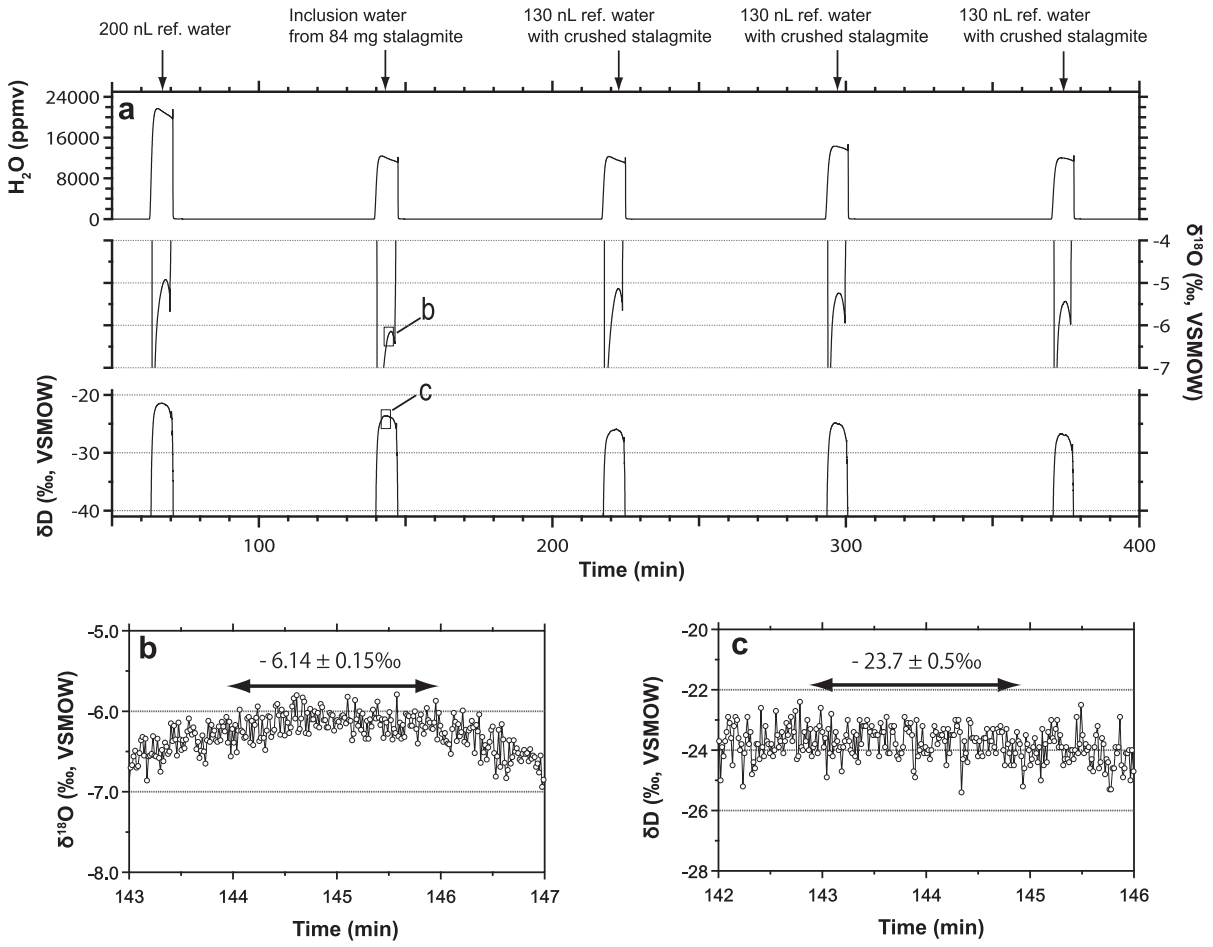

Fig. 2. Inclusion water isotopic measurement sequence. (a) A sequence of water vapor concentration (upper panel), $\delta^{18}O$ (middle panel), and δD (lower panel) measurements, including one reference water OK11, one stalagmite sample, and three OK11 reference water sample. The example presented here is for subsample GYK2-L4b. Records are plotted for data smoothed over 60 s. Enlarged 4-min windows of raw (b) $\delta^{18}O$ and (c) δD data. Two-minute plateau data were used to calculate the isotopic ratio, which was expressed as an average ± 1σ.

$\delta^{18}O$ due to the sorption of injected water onto the freshly crushed calcite surface [also see Dennis et al. (2001) for similar tests]. However, a small but significant isotopic bias exists for δD. The correction for this adsorption effect for δD is given in Section 3.1.3.

2.4. Correction for memory effect

For oxygen and hydrogen isotopic measurements of water, previous studies (Olsen et al., 2006; Gupta et al., 2009; Gröning, 2011) noted an inevitably significant instrumental memory effect requiring correction. The measured isotopic value of the current i_{th} injection, $\delta_{CM,i}$, can be written as follows:

$$\delta_{CM,i} = X \cdot \delta_{PT} + (1 - X)\delta_{CT} \quad (2)$$

where X is the memory coefficient of the i_{th} injection, δ_{CT} is the true value of the current water sample, and δ_{PT} is the true value of the previous water sample. Practically, $X = (\delta_{CM,\ i} - \delta_{CT})/(\delta_{PT} - \delta_{CT})$ can be estimated by replicate laboratory standard measurements until the memory effect decreases significantly. To estimate the value of X, three laboratory standards, OK11, DW11 ($\delta^{18}O = -8.54‰$ and $\delta D = -56.02‰$) and SEA11 ($\delta^{18}O = -0.04‰$ and $\delta D = 0.50‰$) were injected sequentially. Different aliquots of the water standards (30–250 nL) were used to estimate the dependence of the X value on sample volume (e.g., Olsen et al., 2006).

Before fluid inclusion measurements, the OK11 reference water was measured 4–6 times to obtain the value of δ_{PT}. Because the δ values depend on the mixing ratio, the volume of water used for the δ_{PT} measurement should match that of the subsequent fluid inclusion measurement. The water content of the stalagmite sample can be estimated in advance by measuring the pressure of the inclusion water released from the stalagmite fragments of 20–100 mg that were collected when the subsamples were cut from each layer. In this study, the difference between the estimated and measured volume of water was 18 ± 36% for the samples. The measured data, $\delta_{CM,\ 1}$, were corrected using the estimated X and δ_{PT}. Then, the δ_{CT} value was calculated using Eq. (2).

2.5. Sample

2.5.1. Stalagmite and farmed calcite samples

Gyokusen Cave (26° 8′ 26″N, 127° 44′ 57″E, 45 m in elevation) is located on Okinawa Island, Japan, on the eastern border of the East Asian subtropical monsoon region. An artificial entrance to this 5 km-long cave was excavated for tourists in 1972. The modern annual mean (2010–2014) air temperatures recorded at three nearby meteorological stations (within a 10-km distance) were 21.3 ± 0.2 °C (1σ, hereafter), 23.1 ± 0.2 °C, and 23.3 ± 0.2 °C at Itokazu (186 m in elevation), Naha (28 m in elevation), and Ashimine (3 m in elevation), respectively.

Two calcite stalagmites, GYK7 and GYK8 (Fig. 3), were collected in one chamber located 150 m from the artificial entrance and 900 m from the natural entrance. Another stalagmite, GYK2, was collected at a site 300 m from the artificial entrance and 700 m from the natural entrance. Modern active calcite samples ($n = 14$) were collected on glass plates at the stalagmite GYK8 point every 1–2 months from June 2011 to December 2012. The relative humidity in the two chambers was 95–100%, and the mean annual (2010–2012) temperature o at GYK7 and GYK8 sites was 23.4 ± 0.5 °C.

Stalagmite GYK2 was cut into quarters, and GYK7 and GYK8 were halved. In total, eight subsamples of the three stalagmites (Fig. 3) were dated using U–Th techniques (Shen et al., 2003, 2012). Four powdered subsamples were drilled from GYK2 (Fig. 3a). Two chipped subsamples were taken from both GYK7 and GYK8 (Fig. 3b and c). The chipped subsamples (100–277 mg) were crushed into 10- to 30-mg segments and physically cleaned by ultrasonication with deionized water 4–5 times (Shen et al., 2008). Chemical preparation (Shen et al., 2003) was performed on a class-100 clean bench in a class-10,000 clean room. U–Th isotopic compositions and concentrations (Table 1)

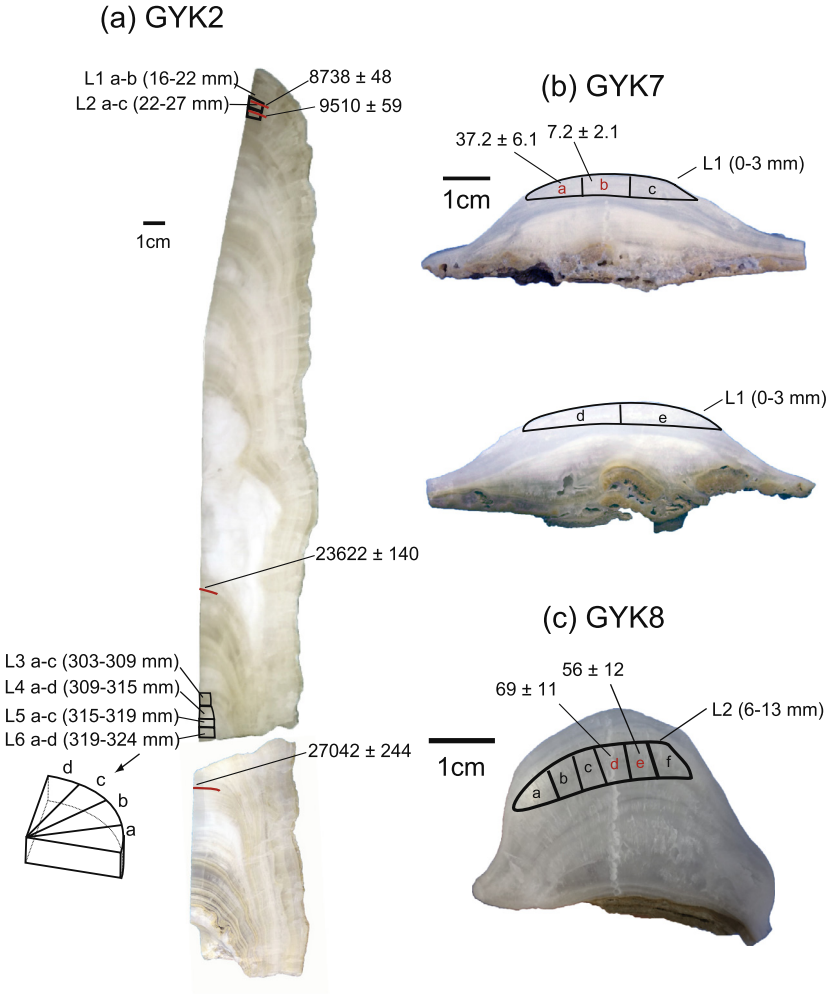

Fig. 3. Photographs of three stalagmites collected from Gyokusen Cave. (a) From a quartered section of stalagmite GYK2, six layers, L1–L6, were taken and cut into 1–4 wedge-shaped chipped subsamples, as indicated in the schematic illustration for L6. (b) For the halved GYK7 stalagmites, five subsamples, L1-a to L1-e, were taken from both sides. (c) For half section of stalagmite GYK8, one layer of GYK8-L2 was cut into six subsamples. Carbonate $\delta^{18}O$ and $\delta^{13}C$ and inclusion water $\delta^{18}O$ and δD were measured for all subsamples. The U–Th dates (unit: year ± 2σ) of the layers and subsamples shown in red were determined. The horizontal bars represent 1 cm. (For interpretation of the references to color in this figure legend, the reader is referred to the web version of this article.)

Table 1
Uranium and thorium isotopic compositions and ages of stalagmite subsamples determined by MC-ICP-MS at the HISPEC, National Taiwan University.

ID	Depth from top (mm)	Weight (g)	^{238}U ppb	^{232}Th ppt	δ^{234}U measured[a]	$[^{230}Th/^{238}U]$ activity[c]	$[^{230}Th/^{232}Th]$ ppm[d]	Age uncorrected	Age corrected[c,e]	$\delta^{234}U_{initial}$ corrected[b]
GYK2	18	0.1204	172.52 ± 0.29	127.4 ± 3.9	38.6 ± 2.4	0.08018 ± 0.00037	1790 ± 55	8756 ± 47	8738 ± 48	39.6 ± 2.5
	23.5	0.1304	181.12 ± 0.18	229.6 ± 3.6	40.6 ± 1.5	0.08723 ± 0.00048	1134 ± 19	9542 ± 56	9510 ± 59	41.7 ± 1.5
	252	0.162	69.94 ± 0.14	101.1 ± 2.9	20.6 ± 2.7	0.19920 ± 0.00089	2271 ± 65	23,659 ± 138	23,622 ± 140	22.0 ± 2.9
	335.5	0.1149	171.24 ± 0.31	1841.7 ± 5.8	21.1 ± 2.4	0.2265 ± 0.0014	347.2 ± 2.3	27,320 ± 201	27,042 ± 244	22.8 ± 2.6
GYK7-L1-a	0–3	0.27678	546.05 ± 0.69	246.0 ± 1.7	10.6 ± 1.5	0.000454 ± 0.000015	16.60 ± 0.58	49.0 ± 1.7	37.2 ± 6.1	10.6 ± 1.5
GYK7-L1-b	0–3	0.21783	644.76 ± 0.89	79.9 ± 2.1	8.3 ± 1.6	0.000097 ± 0.000012	12.9 ± 1.7	10.5 ± 1.3	7.2 ± 2.1	8.3 ± 1.6
GYK8-L2-d	6–13	0.1158	142.48 ± 0.17	51.3 ± 4.0	7.0 ± 1.5	0.00072 ± 0.00010	33.0 ± 5.1	78 ± 10	69 ± 11	7.0 ± 1.5
GYK8-L2-e	6–13	0.10035	148.49 ± 0.17	17.6 ± 4.6	5.2 ± 1.4	0.00055 ± 0.00011	76 ± 25	59 ± 11	56 ± 12	5.2 ± 1.4

Chemical analyses (Shen et al., 2003) were performed in December 2013, and the instrumental analyses were performed using MC-ICP-MS (Shen et al., 2012).
Analytical errors are 2σ of the mean.

[a] $[^{238}U] = [^{235}U] \times 137.818$ (±0.65‰) (Hiess et al., 2012); $\delta^{234}U = ([^{234}U/^{238}U]_{activity} - 1) \times 1000$.

[b] $\delta^{234}U_{initial}$ corrected was calculated based on ^{230}Th age (T), i.e., $\delta^{234}U_{initial} = \delta^{234}U_{measured} \times e^{\lambda 234 \times T}$, and T is the corrected age.

[c] $[^{230}Th/^{238}U]$ activity $= 1 - e^{-\lambda 230 \times T} + (\delta^{234}U_{measured}/1000)[\lambda_{230}/(\lambda_{230} - \lambda_{234})](1 - e^{-(\lambda 230 - \lambda 234) T})$, where T is the age. The decay constants are 9.1705×10^{-6} yr^{-1} for ^{230}Th, 2.8221×10^{-6} yr^{-1} for ^{234}U (Cheng et al., 2013), and 1.55125×10^{-10} yr^{-1} for ^{238}U (Jaffey et al., 1971).

[d] The degree of detrital ^{230}Th contamination is indicated by the $[^{230}Th/^{232}Th]$ atomic ratio instead of the activity ratio.

[e] Age corrections (relative to chemistry date) for samples were calculated using an estimated atomic $^{230}Th/^{232}Th$ ratio of 4 ± 2 ppm. These are the values for a material at secular equilibrium, with a crustal $^{232}Th/^{238}U$ of 3.8 with an arbitrary uncertainty of 50%.

were determined using a multi-collection inductively coupled plasma mass spectrometer (MC-ICP-MS), NEPTUNE, Thermo-Fisher, at the High-Precision Mass Spectrometry and Environment Change Laboratory (HISPEC) of the Department of Geosciences at National Taiwan University (Shen et al., 2012). The uncertainties of the U–Th ages relative to the chemistry date, December 2013, are two standard deviations (2σ).

For carbonate δ^{18}O analyses, 29 powdered subsamples (19 from six layers of GYK2, five from one layer of GYK7, and five from one layer of GYK8) were extracted from the same layers for water inclusion analysis (Table 2 and Fig. 3). Six coeval subsamples were drilled at 20.5, 24.5, 306.5, 313.0, 317.5, and 321.5 mm from the top of stalagmite GYK2 for the Hendy Test (Hendy, 1971) to evaluate whether the formations were deposited under oxygen isotopic equilibrium conditions. The collected glass plate calcite samples were also measured.

Stalagmite carbonate subsamples were measured using an isotope ratio mass spectrometer (IRMS, Thermo DELTA V Advantage) equipped with a Thermo Gasbench II system at the University of the Ryukyus. Powdered subsamples of 150–200 μg were reacted with 100% phosphoric acid at 72 °C in septa-capped vials before measuring the released CO_2. The δ^{18}O value for carbonate is relative to the Vienna Pee Dee Belemnite (VPDB) standard unless otherwise noted. The 1σ reproducibility for the analysis of the carbonate standard NBS19 over six months was ±0.04‰ for δ^{18}O and ±0.03‰ for δ^{13}C.

Coeval subsamples were prepared to evaluate the reproducibility of the inclusion water measurements. Chips (200–1500 mg) were subsampled from six layers of GYK2, one layer of GYK7, and one layer of GYK8 (Fig. 3). Each chip was cut into 2–5 coeval subsamples with weights of 77–286 mg for the isotopic measurements of the water (Table 2).

2.5.2. Rainfall and drip water samples

A 20-ml bottle of drip water was collected every 1–2 months from beneath 15–20 stalactites located <5 m from the GYK7 and GYK8 sites (called "site A"); Thirty-one bottles were gathered from February 2010 to December 2012. Drip water samples ($n = 24$) were collected every 1–2 months from June 2010 to December 2012 under one stalactite located 15 m from the GYK8 site (called "site B"). Local rainfall samples were collected every week from April 2011 to July 2012 for the δ^{18}O and δD measurements.

The δ^{18}O and δD values of the drip water and rainfall samples were determined using a Picarro L2120-i CRDS equipped with a V1102-i evaporator at the University of the Ryukyus. The uncertainty of the working water standard OK11 over the analysis course was ±0.08‰ for δ^{18}O and ±0.26‰ for δD. To evaluate possible interference by organic material, 16 drip water samples were also measured by conventional IRMS with an equilibration method (Uemura et al., 2007) at the National Institute of Polar Research (NIPR), Japan, and at the Japan Oil, Gas and Metals National Corporation (JOGMEC). The 1σ analytical precision of the IRMS was ±0.05‰ for δ^{18}O and ±0.5‰ for δD.

Table 2
Reproducibility tests for the δD and $\delta^{18}O$ values of inclusion water and the $\delta^{18}O$ and $\delta^{13}C$ values of calcite.

ID		$CaCO_3$ (mg)	Vapor (ppmv)	Water amount (nL)	$H_2O/CaCO_3$ (nL/mg)		Inclusion water		Stalagmite calcite		T (°C)	ΔT (°C, relative to modern)
							δD (‰, VSMOW)	$\delta^{18}O$ (‰, VSMOW)	$\delta^{18}O$ (‰, VPDB)	$\delta^{13}C$ (‰, VPDB)		
GYK2												
L1	a	84	6964	70	0.77		−24.5	−6.15	−5.55	−12.96	18.5	−3.9
L2	c	173	6679	70	0.38		−23.1	−5.88	−5.47	−12.02	19.5	−3.0
L3	b	93	8072	80	0.86		−23.0	−5.79	−4.26	−12.35	14.1	−8.4
	c	87	5477	50	0.57		−23.0	−5.57	−4.23	−11.45	14.9	−7.5
						Mean	−23.0	−5.68	−4.25	−11.90	14.5	−7.9
						SD	±0.0	±0.15	±0.02	±0.64	±0.6	±0.6
L4	a	85	26,062	240	2.82		−29.3	−6.12	−3.67	−10.66	9.8	−12.7
	b	84	11,620	130	1.55		−27.7	−6.06	−4.05	−11.07	11.8	−10.7
	c	77	19,481	200	2.60		−29.7	−6.60	−3.91	−10.79	8.6	−13.8
	d	99	17,329	180	1.82		−26.6	−6.17	−3.85	−11.00	10.3	−12.1
						Mean	−28.3	−6.24	−3.87	−10.88	10.1	−12.3
						SD	±1.5	±0.25	±0.16	±0.19	±1.3	±1.3
L5	a	112	18,681	180	1.61		−30.3	−6.38	−4.16	−11.36	10.8	−11.7
	b	121	26,287	260	2.15		−33.1	−6.32	−4.20	−11.68	11.2	−11.2
	c	114	23,658	230	2.02		−32.9	−6.41	−3.85	−10.64	9.2	−13.2
						Mean	−32.1	−6.37	−4.07	−11.23	10.4	−12.0
						SD	±1.6	±0.05	±0.19	±0.53	±1.1	±1.1
L6	a	116	12,518	140	1.21		−26.5	−5.34	−4.68	−12.15	18.3	−4.2
	b	124	22,905	210	1.69		−32.8	−6.48	−4.42	−12.02	11.5	−10.9
	c	87	19,392	200	2.30		−32.4	−6.34	−4.37	−12.15	11.9	−10.5
	d	104	15,086	160	1.54		−30.1	−5.91	−4.58	−11.34	15.0	−7.5
						Mean	−30.4	−6.02	−4.51	−11.92	14.2	−8.3
						SD	±2.9	±0.51	±0.15	±0.39	±3.1	±3.1
GYK7												
L1	a	286	9762	100	0.35		−41.7	−6.61	−6.43	−7.24	20.6	−1.9
	b	236	6069	60	0.25		−40.0	−6.71	−6.51	−7.19	20.5	−1.9
	c	239	8102	80	0.33		−37.6	−5.42	−6.50	−7.34	27.0	4.6
	e	256	7792	80	0.31		−40.7	−6.62	−6.62	−7.57	21.5	−0.9
						Mean	−40.0	−6.34	−6.51	−7.34	22.4	0.0
						SD	±1.7	±0.61	±0.08	±0.17	±3.1	±0.6
GYK8												
L2	a	203	12,824	130	0.64		−34.1	−5.99	−6.26	−5.99	22.8	0.4
	c	162	10,293	100	0.62		−32.1	−6.20	−6.47	−5.43	22.8	0.4
	d	219	13,521	140	0.64		−35.1	−6.19	−5.92	−6.29	20.1	−2.3
	e	171	12,618	120	0.70		−32.4	−5.72	−6.25	−5.66	24.2	1.8
	f	157	10,200	100	0.64		−33.2	−5.98	−6.13	−6.66	22.3	−0.2
						Mean	−33.4	−6.02	−6.20	−6.01	22.5	0.0
						SD	±1.3	±0.20	±0.20	±0.49	±1.5	±1.5

The variation of each layer is shown with standard deviation (1σ). Water amounts of GYK2-L1b, L2a, L2b, L3a, and GYK7L1-d were below the limit of quantification (<50 nL). GYK8-L2b was used for a different experiment. Temperature was calculated using a oxygen isotope fractionation factor (Coplen, 2007).

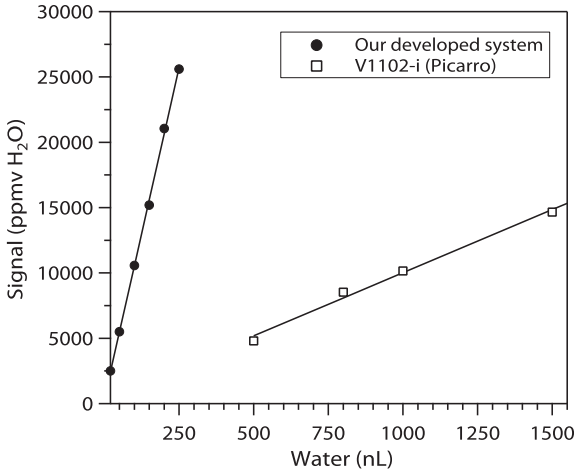

Fig. 4. Comparison of the sensitivities of our device and a commercial evaporator. The plot of the generated water vapor level (ppmv) versus the injection volume illustrates the different sensitivities of the device (circles) and a commercial evaporator, V1102-i (Picarro Inc.) (squares). A high concentration of 10,000 ppmv can, for example, be produced using only 100 nL of water in our developed system, while the V1102-I evaporator requires a volume of 1000 nL.

3. RESULTS AND DISCUSSION

3.1. Performance evaluation of the developed techniques

3.1.1. Liquid water injection test

The sensitivity of the water vapor content is plotted in Fig. 4. Our evaporation device produced sufficient vapor concentrations using small volumes of liquid water. The vapor level of 10,000 ppmv generated from only 100 nL of water was 10 times higher than that generated by the commercial evaporator Picarro V1102-i. This improved sensitivity was achieved by a combination of small gas expansion chamber and low N_2-gas dilution pressure (Fig. 1).

3.1.2. Memory effect

The memory effect of the first to third injections is illustrated in Fig. 5. The memory coefficient, X, decreased exponentially as reference water was sequentially injected. At 150 nL, the X values of the first injection were 29.3 $\pm$ 2.3% for δD and 6.9 $\pm$ 0.9% for $\delta^{18}O$. The memory effect of δD was four times larger than that of $\delta^{18}O$, similar to the observations from the CRDS system (Gupta et al., 2009). A 6.9% memory for $\delta^{18}O$, for example, can result in a bias of 0.069‰ in the first injection, $\delta_{CM,\ 1}$, if the difference between the true values, $\delta_{PT} - \delta_{CT}$, is 1‰.

For $\delta^{18}O$, the X values of the first injection increased from 7% to 23% as the volume of water decreased from 150 nL to 30 nL (Fig. 5a). This memory effect trend for the first injection can be described using an empirical exponential equation ($X = 0.047\ nL^{-0.234}$, $R^2 = 0.88$) for water volumes of 50–250 nL. The trends for second and third injections were not significant (Fig. 5a); thus, average values of 3.9% and 2.4% were used. For δD, the systematic trends of X were significant (Fig. 5b). The largest value of

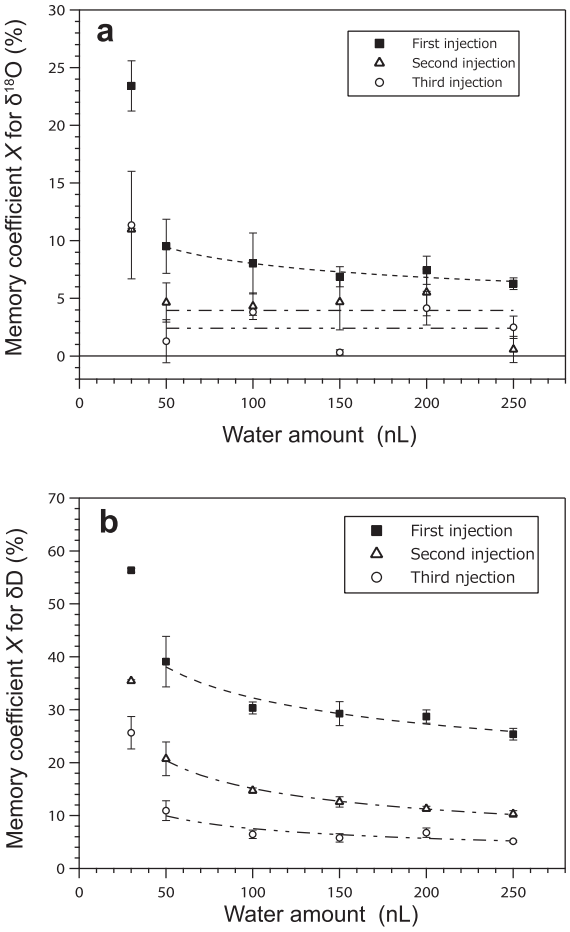

Fig. 5. Memory coefficient for $\delta^{18}O$ and δD against the amount of water. (a) Memory coefficient, X, for the first (solid square), second (triangle), and third (circle) injections. Error bars represent the standard deviation of the mean. The dashed line is the best fit curve for the X values of the first injection. The chain and two-dot chain lines are average X values of the second and third injections. (b) Same as panel (a) but for δD. Dashed, chain, and two-dot chain lines represent the best fit curves for the X values of the first, second, and third injections, respectively.

56.3% was observed at the lowest volume of water, 30 nL. The X values for the first, second and third injections can be best described by exponentially fitting the volumes of water from 50 to 250 nL. The empirical curves are $X = 0.186\ nL^{-0.239}$ ($R^2 = 0.93$), $X = 0.056\ nL^{-0.430}$ ($R^2 = 1.00$), and $X = 0.030\ nL^{-0.402}$ ($R^2 = 0.78$), for the first, second, and third injections, respectively.

3.1.3. Water adsorption test

Inclusion water $\delta^{18}O$ and δD measurements can be biased by the adsorption of water on the carbonate surface (Dennis et al., 2001). We evaluated the influence of this effect by measuring the $\delta^{18}O$ and δD values of the reference water, OK11, for different water/calcite ratios. Different volumes of reference water (20–300 nL) were injected through the injection port with granulated and dried stalagmite subsamples placed in the crushing device. The injected water vapor interacted with the dried stalagmite

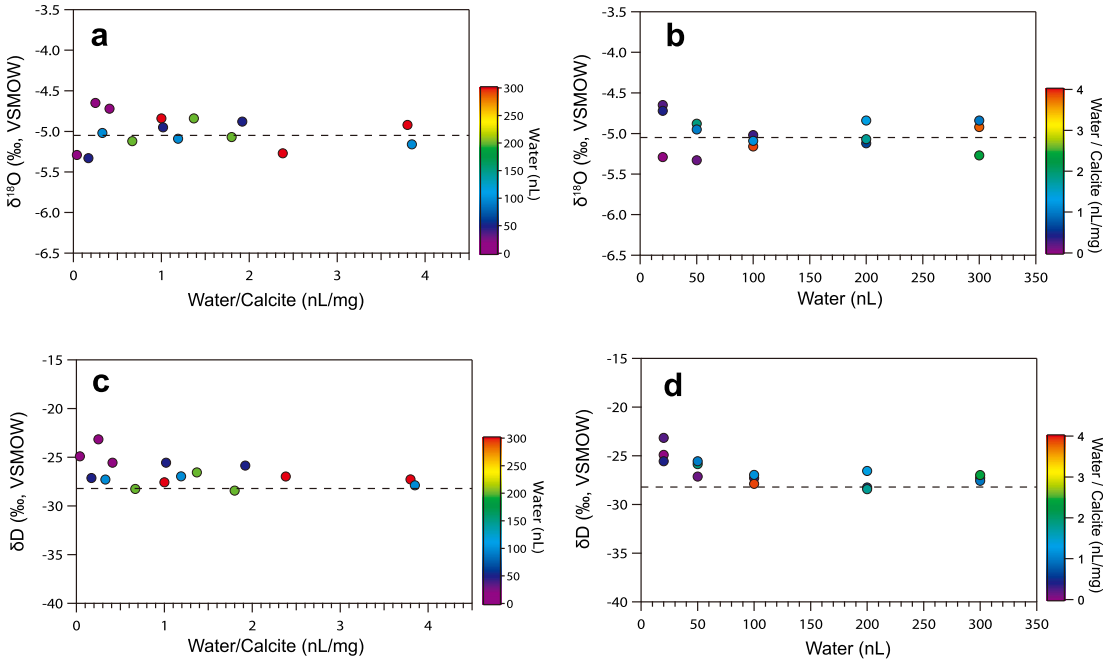

Fig. 6. Reproducibility tests of the isotope analyses with different water/calcite ratios and water volumes. (a) A plot of $\delta^{18}O$ versus the water/calcite ratio (nL/mg). Colored symbols denote different injected volumes (nL) of the reference water OK11. (b) A plot of $\delta^{18}O$ versus the injected reference water volume (nL). The colored symbols represent different water/calcite ratios (nL/mg; colored bar). (c) and (d) Same as panels (a) and (b) but for δD. The horizontal dashed lines are the isotopic ratios of the reference water OK11. (For interpretation of the references to color in this figure legend, the reader is referred to the web version of this article.)

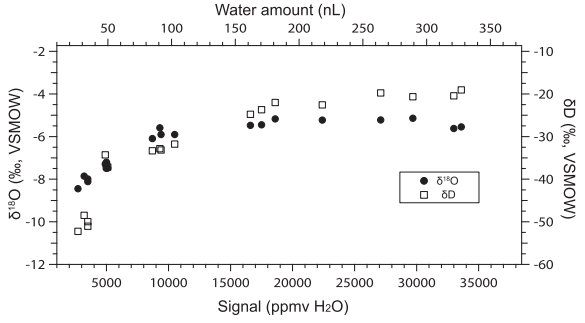

Fig. 7. Relationship between the measured $\delta^{18}O$ and δD values and the vapor concentration. Significant decreasing trends of raw $\delta^{18}O$ (circles) and δD (squares) data, particularly for water vapor levels <10,000 ppmv, should be corrected. The equivalent amount of water (nL) is given in the upper *X*-axis.

(26–483 mg) for 2 min. The trap chamber was maintained at 150 °C to prevent the adsorption of vapor to the chamber surface. Then, the vapor was trapped cryogenically for processing as described in Section 2.2.

The results from evaluating the influences of the adsorption of the working reference water OK11 onto the granulated calcite are illustrated in Fig. 6. The $\delta^{18}O$ values under different water/calcite ratios (0.04–3.85 nL/mg) and volumes of water (20–300 nL) are plotted in Fig. 6a and b, respectively. The overall variability of multiple water measurements ($n = 15$) was ±0.21‰ for $\delta^{18}O$ over the entire range of water/calcite ratios. Linear and second-order polynomial fittings did not yield significant correlations ($R^2 < 0.05$ for both the water/calcite ratio and the volume of water). Thus, the measured water $\delta^{18}O$ value does not depend on the water/calcite ratio or on the volume of water. No significant adsorption effect was observed, even for water/calcite ratios <1 nL/mg.

The δD values of the working reference OK11 are plotted in Fig. 6c and d. Despite correcting for the volume of water (Section 2.3), the δD data clearly exhibit a systematic offset for sample volumes <50 nL (Fig. 6d). A second-order polynomial fitting ($\delta D = 9.87 \times 10^{-5}\ x^2 - 3.97 \times 10^{-2}\ x - 24.13$, where x is the volume of water in nL) indicated a significant correlation ($R^2 = 0.69$) between δD and the volume of water. The measured δD values were corrected for this adsorption effect using polynomial fitting. The 1σ variability of the corrected δD data was ±0.8‰ ($n = 15$) over the entire range of water/calcite ratios.

The worst reproducibility, ±0.35‰ for $\delta^{18}O$ and ±1.2‰ for δD, was observed for the smallest volume of water (20 nL, equivalent to 3000 ppmv) (Fig. 6). This low reproducibility can be attributed to the isotopic dependency on the vapor content (e.g., Brand et al., 2009; Arienzo et al., 2013) and the correction scheme described in Section 2.3. The relationship between the measured raw $\delta^{18}O$ and δD data and the water vapor concentration of OK11 water over a five-day course in April 2014 is presented in Fig. 7. No significant difference was observed in the measured $\delta^{18}O$ data for water vapor contents >10,000 ppmv, but the $\delta^{18}O$ value decreased with a slope of 0.37‰/1000 ppmv for water levels <10,000 ppmv. In addition, the measured δD value decreased with a slope of 2.6‰/1000 ppmv when the water level was <10,000 ppmv. These steep decreasing

trends increase the uncertainty of the corrected isotope ratios.

3.1.4. Spectral interference

Recent studies have suggested that organic contaminants can interfere with CRDS measurements (West et al., 2010; Schultz et al., 2011; Zhao et al., 2011). Speleothems can be deposited with organic material (McGarry and Baker, 2000; Blyth et al., 2008) and gases, including N_2, O_2, CO_2, CH_4 and noble gases, which can be released by the thermal decomposition of carbonate (Verheyden et al., 2008). Drip water also contains complex organic compounds, such as humic and fulvic acid colloidal molecules (e.g., Tatár et al., 2004).

The differences between CRDS drip water isotopic data measurements and conventional IRMS data measurements were $+0.07 \pm 0.08$‰ ($n = 16$) for $\delta^{18}O$ and $+0.1 \pm 0.4$‰ for δD ($n = 7$). The experimental results indicated that this interference was insignificant for our inclusion measurements. In addition, the amount of gas emitted from the stalagmites during the −75 °C purification process (Section 2.3) was <0.2 Pa, extremely small compared with the range of 71.5–616.0 Pa for the samples. The contamination indices, including CH_4, the baseline shift, and the slope shift of the CRDS analyzer, did not differ significantly between the fluid inclusion and reference water measurements. Therefore, spectral interference did not significantly bias the isotopic analyses of our stalagmite inclusion water samples.

3.1.5. Reproducibility of the inclusion water measurements

The volume of water released from the stalagmite samples (77–286 mg) ranged from 20 to 260 nL. Compared with typical water content values of 0.01–0.5 wt% (Schwarcz et al., 1976; McDermott et al., 2005), the water contents of our samples (0.03–0.28 wt%) were intermediate. Because the evaluation of the memory effect (Fig. 5), the adsorption of water onto carbonate surfaces (Fig. 6), and the dependence of isotope ratios on the volume of water (Fig. 7) indicated large errors when aliquots of water <50 nL were analyzed, we considered 50 nL the limit of quantitation. Measured isotopic data for speleothem samples using less than 50 nL of water are not reliable. Thus, five of the 29 subsamples with water volumes <50 nL (Table 2) were excluded.

Stable hydrogen and oxygen isotopic measurements of coeval stalagmite subsamples are summarized in Table 2. The magnitudes of the corrections for the memory effect, $\delta_{CT} - \delta_{CM,1}$, ranged from −0.20 to −0.02‰ (−0.10‰ on average) for $\delta^{18}O$ and from −4.9 to 2.1‰ (−0.9‰ on average) for δD. The 1σ reproducibility values of each layer ranged from 0.05 to 0.61‰ for $\delta^{18}O$ and from 0.0 to 2.9‰ for δD (Table 2). The overall average reproducibility of the repeated stalagmite measurements was ±0.33‰ for $\delta^{18}O$ and ±1.6‰ for δD. This $\delta^{18}O$ precision is superior to the value of ±0.5‰ that reported for a recently developed CRDS method (Arienzo et al., 2013) and is comparable to the value of ±0.3–0.5‰ obtained using IRMS techniques (Dennis et al., 2001; Vonhof et al., 2006; Dublyansky and Spotl, 2009). The precision of the δD analysis was comparable to previously observed precisions of ±1.5–3‰ (Dennis et al., 2001; Vonhof et al., 2006; Dublyansky and Spotl, 2009; Arienzo et al., 2013).

One of the most important advantages of our developed technique is its reliance on a small sample size of 50–260 nL, which is considerably smaller than the sample sizes of 0.1–1.0 μL used in previous IRMS techniques (Dennis et al., 2001; Vonhof et al., 2006; Dublyansky and Spotl, 2009) and 0.4–1.2 μL used in previous CRDS techniques (Arienzo et al., 2013; Affolter et al., 2014). However, a routine measurement time of 7 h is required for a full measurement sequence, which is longer than the 1–2 h required for the previously described CRDS method (Arienzo et al., 2013). The reproducibility of the $\delta^{18}O$ and δD measurements of speleothem inclusion water could be specimen and site specific due to the diversity of speleothem microdomain structures and inclusion formation (e.g., Dennis et al. (2001)).

3.1.6. Comparison of the speleothem inclusion water and modern drip water

The accuracy of our analytical method was evaluated by comparing the isotopic composition of modern drip water with that of inclusion water from active stalagmite deposition. The isotope ratios of the drip water, inclusion water, and rainfall are presented in Fig. 8. The arithmetic $\delta^{18}O$ average of the drip water samples collected at site A was -5.37 ± 0.18‰. The mean (February 2010–December 2012) of all drip water $\delta^{18}O$ data, which ranged from −6.20‰ to −5.01‰, was -5.59 ± 0.29‰. The δD values

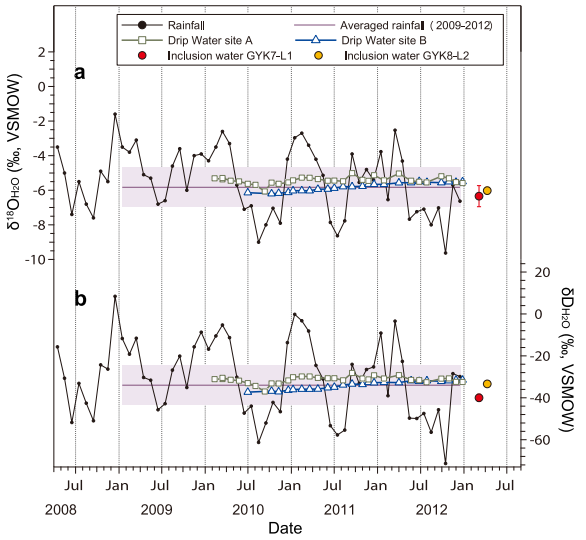

Fig. 8. Oxygen and hydrogen isotope ratios of rainfall, drip water, and inclusion water. (a) $\delta^{18}O$ data for monthly rainfall [data during April 2008–March 2011 from Uemura et al. (2012)] (black line), drip water samples at site A (squares) and site B (triangles), and inclusion water samples of stalagmite GYK7-L1 (red circle) and GYK8-L2 (orange circle). The horizontal zone with dashed purple lines indicates the weighted average precipitation $\delta^{18}O$ (AD 2009–2012) with 2σ variability. (b) Same as panel (a) but for δD. (For interpretation of the references to color in this figure legend, the reader is referred to the web version of this article.)

varied from −28.2‰ to −37.3‰, with an average of −32.5 ± 2.2‰. These results are consistent with the rainfall-weighted annual (2009–2012) averages of −5.83 ± 0.57‰ for $\delta^{18}O$ and −34.0 ± 4.7‰ for δD.

Contemporary (2010–2012) $\delta^{18}O$ and δD values of inclusion water for active stalagmite deposition with a thickness of <0.06 mm are not measureable. The two most recently measured layers are GYK7-L1 and GYK8-L2, which have U–Th dates of 7–37 and 56–69 years, respectively (Table 1). The $\delta^{18}O$ values of inclusion water samples were −6.34 ± 0.61‰ for GYK7-L1 and −6.02 ± 0.20‰ for GYK8-L2 (Fig. 7a). Considering that the $\delta^{18}O$ variability of annual mean precipitation is ±0.57‰, the slight offsets of −0.75 ± 0.68‰ and −0.43 ± 0.35‰, respectively, from drip water values are insignificant.

The δD data for the inclusion water were −40.0 ± 1.7‰ for GYK7-L1 and −33.4 ± 1.3‰ for GYK8-L2 (Fig. 7b). Considering that the δD variability of annual mean precipitation is ±4.7‰, the respective differences, −7.5 ± 2.8‰ and 0.8 ± 2.5‰, from mean drip water were insignificant. A reported analytical offset between inclusion water and drip water values of 20–30‰ for δD for thermal decomposition method (Yonge, 1982; Goede et al., 1986; Matthews et al., 2000; McGarry et al., 2004) was not observed. Our results are consistent with recent studies that have reported that the values of the $\delta^{18}O$ and δD for inclusion water correspond well with the cave drip water values (Dennis et al., 2001; Genty et al., 2002; Fleitmann et al., 2003; Demeny and Siklosy, 2008; van Breukelen et al., 2008; Zhang et al., 2008; Dublyansky and Spotl, 2009; Griffiths et al., 2010).

Comparison of stable isotope ratios between drip water observation and fluid inclusion analysis is limited by their natural spatial and temporal variabilities. Arienzo et al. (2013) reported an inter-laboratory difference of 0.7‰ for $\delta^{18}O$ and 2.5‰ for δD for speleothem inclusion water analysis. Such discrepancies could be attributed to decrepitation during heat drying process (e.g., Dublyansky and Spotl, 2009) or isotope exchange between inclusion water and host calcite. A systematic inter-laboratory calibration program with diverse stalagmite types should be conducted to minimize any possible technical biases.

3.2. Application to paleoclimate reconstruction

3.2.1. Hendy test

Coeval $\delta^{13}C$ and $\delta^{18}O$ data for six layers of the stalagmite GYK2 are plotted in Fig. 9a. For layers L1, L2, L3, and L6, only small $\delta^{18}O$ variations of ±0.12–0.14‰ (±1σ)

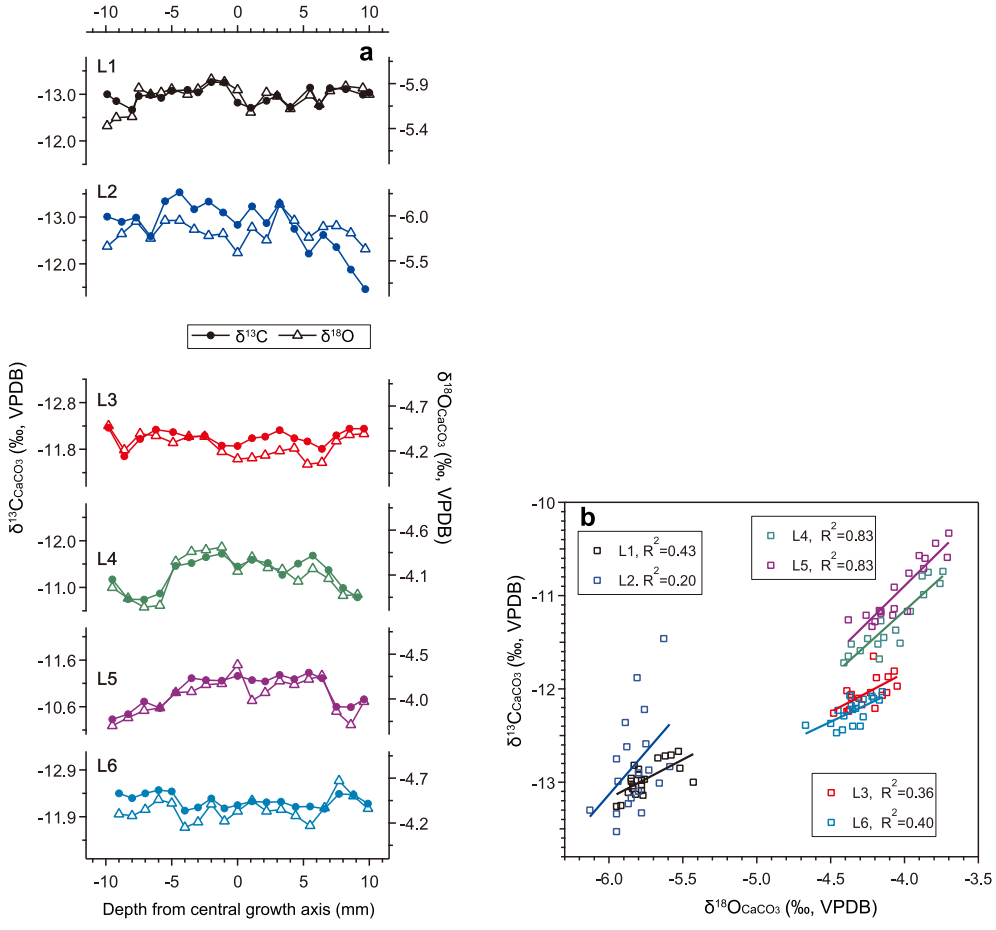

Fig. 9. Hendy test for the GYK2 stalagmites. (a) Coeval subsample $\delta^{13}C$ (circles) and $\delta^{18}O$ (triangles) data for six layers: L1 (black), L2 (dark blue), L3 (red), L4 (green), L5 (purple), and L6 (light blue). (b) Correlations between the $\delta^{13}C$ and $\delta^{18}O$ data with regression lines and coefficients. (For interpretation of the references to color in this figure legend, the reader is referred to the web version of this article.)

were observed despite the relatively large $\delta^{13}C$ variations of ±0.14–0.53‰. Although correlations ($R^2 = 0.20$–0.43) of coeval $\delta^{18}O$ and $\delta^{13}C$ data were observed (Fig. 9b), the small $\delta^{18}O$ variations of indicate that the carbonates were deposited at near an oxygen isotope equilibrium conditions and less affected by kinetic effects.

For layers L4 and L5 of the stalagmite GYK2, clear enrichment trends of approximately 0.5‰ for $\delta^{18}O$ and 1.0‰ for $\delta^{13}C$ occurred outward at distances of 5–7 to 10 mm from the central growth axis (Fig. 9a). The strong $\delta^{13}C$–$\delta^{18}O$ correlations (Fig. 9b) for L4 ($\delta^{13}C = 1.42 \times \delta^{18}O - 5.5$, $R^2 = 0.83$) and L5 ($\delta^{13}C = 1.53 \times \delta^{18}O - 4.7$, $R^2 = 0.83$) demonstrate that the $\delta^{18}O$ and $\delta^{13}C$ values for the marginal subsamples were both significantly affected by kinetic fractionation (e.g., Hendy, 1971; McDermott, 2004; Wiedner et al., 2008; Lachniet, 2009; Mühlinghuas et al., 2009). Different isotope fractionation behaviors between the layers of L3, L4, L5, and L6 suggest that the kinetic effect was variable within several hundred years, probably attributable to changes in precipitation rate (Dietzel et al., 2009; Day and Henderson, 2011) and/or drip interval (Mühlinghuas et al., 2009).

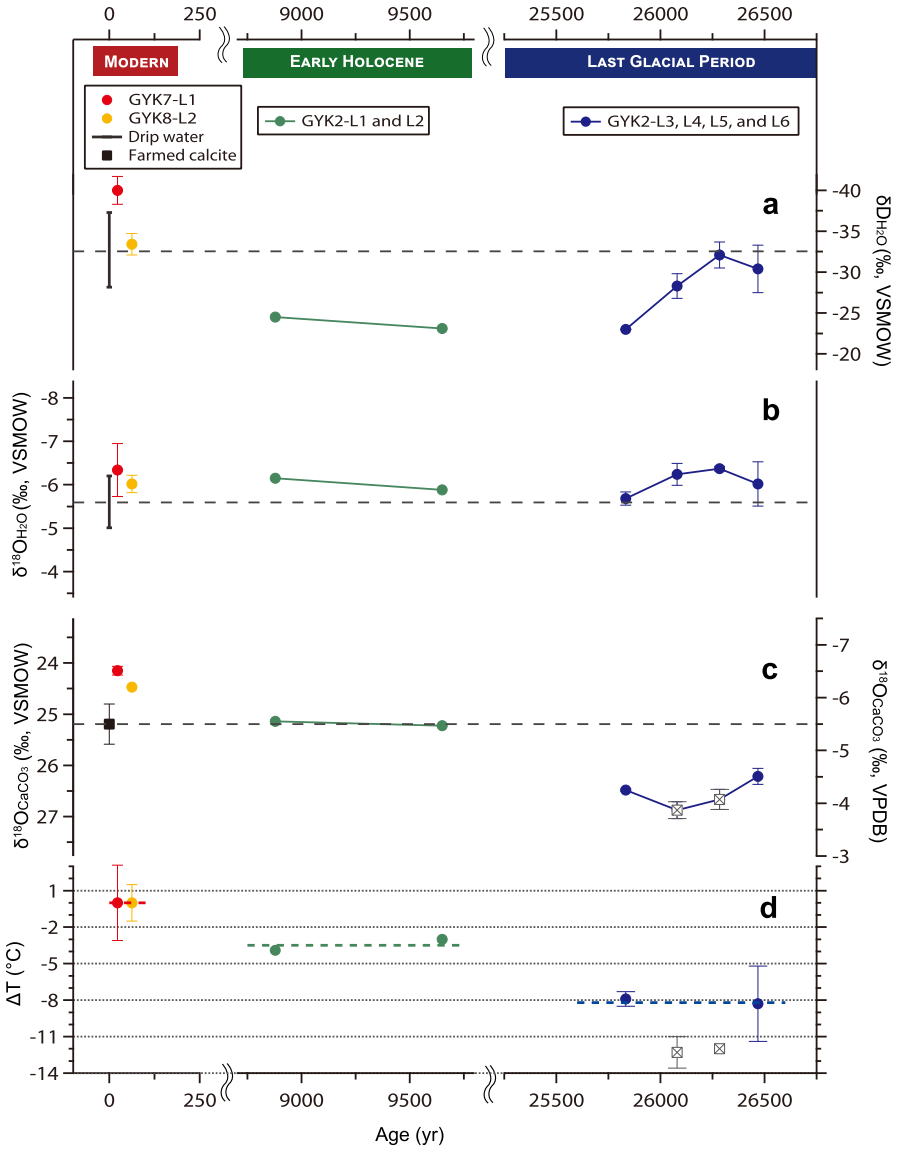

Fig. 10. Oxygen and hydrogen isotope ratios of the inclusion water, coeval stalagmites, and inferred cave paleotemperature. (a) δD and (b) $\delta^{18}O$ values of the inclusion water. (c) Coeval stalagmite $\delta^{18}O$ data. (d) Cave temperature inferred from the coeval $\delta^{18}O$ values of the inclusion water and stalagmites. Red, orange, green, and blue circles denote subsamples of GYK7, GYK8, GYK2-L1–2, and GYK2-L3–6, respectively. The black vertical bars in (a) and (b) are the 1σ ranges of δD and $\delta^{18}O$ for modern drip water. The black squares in (c) and (d) are the $\delta^{18}O$ range and calculated cave temperature for *in situ* farmed calcite, respectively. The hollow squares in (c) and (d) denote the $\delta^{18}O$ values and biased temperature data for the kinetically fractionated stalagmite GYK2-L4 and L-5. The horizontal black dashed lines represent the average isotope ratios of the modern drip water and farmed calcite. The red, green, and blue horizontal dashed lines in panel (d) represent the average temperature values for the modern era, the early Holocene, and the last glacial period, respectively. (For interpretation of the references to color in this figure legend, the reader is referred to the web version of this article.)

For the GYK7-L1 and GYK8-L2 coeval subsamples, a small $\delta^{18}O$ variation of ±0.08–0.20‰ was observed. Combined with the absence of outward shifting from the central growth axis of $\delta^{18}O$ and $\delta^{13}C$ data (Table 2 and Fig. 3), the kinetic fractionation of the two layers is insignificant.

3.2.2. $\delta^{18}O$ data for stalagmite inclusion water and carbonate

The δD and $\delta^{18}O$ data for stalagmite inclusion water and the corresponding values of carbonate $\delta^{18}O$ values are illustrated in Fig. 10. The highest inclusion water δD values of −25 to −23‰ for GYK2-L1 and L2 occurred at 9–10 ka during the early Holocene. These values are approximately 10‰ higher than the values of −40 to −33‰ observed for the decade-old GYK7-L1 and GYK8-L2, and the values of −28 to −37‰ observed for the drip water samples (Fig. 10a). The δD values vary from −32‰ to −23‰ in the four subsamples (GYK2-L3-L6) dated at 26 ka from the last glacial period.

The inclusion water $\delta^{18}O$ data (−6.15‰ for GYK2-L1 and −5.88‰ for GYK2-L2) from the early Holocene are comparable to modern stalagmite and drip water values (Fig. 10b). For the last glacial subsamples (GYK2-L3-L6), the inclusion water $\delta^{18}O$ values varied from −6.37‰ to −5.68‰ and co-varied with the δD data (Fig. 10a and b).

The carbonate $\delta^{18}O$ values obtained from the modern stalagmite subsamples GYK7-L1 and GYK8-L2 were −6.53‰ and −6.20‰, respectively, 0.7–1.0‰ lower than the $\delta^{18}O$ value of the *in situ* farmed calcite of −5.50‰ (Fig. 10c). The early Holocene samples exhibit $\delta^{18}O$ values of −5.62‰ for GYK2-L1 and −5.60‰ for GYK2-L2. The last glacial samples express high $\delta^{18}O$ values of −4.25‰ for GYK2-L3 and −4.51‰ for GYK2-L6. The two glacial layers (GYK2-L4 and L5) exhibited the highest $\delta^{18}O$ values of −3.87‰ and −4.07‰, respectively, which were biased by the kinetic fractionation effect (Section 3.2.1).

The stalagmite inclusion water data provide direct evidence for changes in paleo-rainfall isotope composition. The averaged $\delta^{18}O$ values obtained for the last glacial period insignificantly differ from the modern sample values by 0.05 ± 0.57‰. The glacial seawater ^{18}O was enriched by 0.93‰ due to advancements in the ice sheet (Bintanja and van de Wal, 2008). After correcting for this ice volume factor, the last glacial rainfall $\delta^{18}O$ values are only 0.88 ± 0.57‰ lower than those of the modern samples. An atmospheric general circulation model (Tharammal et al., 2013) and a compilation of proxies and models (Jasechko et al., 2015) revealed a small glacial-modern difference of <2‰ in rain water $\delta^{18}O$ in the region surrounding the Ryukyu Islands. Therefore, the small changes in the inclusion $\delta^{18}O$ data from the last glacial period to modern times are generally consistent with the model and observation.

3.2.3. δD-$\delta^{18}O$ plot for inclusion water

The δD and $\delta^{18}O$ values of inclusion water, drip water, and rain water are plotted in Fig. 11. The local meteoric water line (LMWL) for winter (DJF) ($\delta D = 8.46\ \delta^{18}O + 20.66$, $R^2 = 0.91$) has a larger intercept than for summer (JJA) LMWL ($\delta D = 8.33\ \delta^{18}O + 11.88$, $R^2 = 0.97$). The different local meteoric water lines represent hydrological features in East Asian Monsoon (EAM) systems (Uemura et al., 2012). During the winter, a dry air mass from the continent flows over the warm Kuroshio Current in the East China Sea, and moisture is substantially recharged. This rapid evaporation under low relative humidity conditions over the ocean surface explains the high average *d*-excess value of 19‰ (Merlivat and Jouzel, 1979; Uemura et al., 2008). In the summer, the *d*-excess value is near the global average of 10‰ due to the vapor source of summer precipitation originated from the Western Pacific Warm Pool.

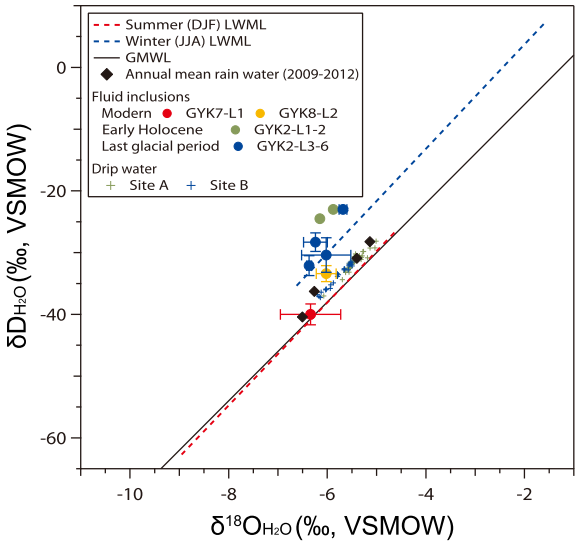

Fig. 11. δD-$\delta^{18}O$ plot of fluid inclusions, drip water and Meteoric Water Lines. Isotope ratios of inclusion water of modern stalagmites GYK7-L1 (red circle) and GYK8-L2 (orange circle), Early Holocene samples GYK2 L1 and L2 (green circles), and the last glacial period samples GYK2 L3–L6 (blue circles). Green and blue crosses indicate drip water data at site A and B, respectively. The dashed red and blue lines are the summer LMWL and winter LMWL, respectively. The black line is the GMWL. (For interpretation of the references to color in this figure legend, the reader is referred to the web version of this article.)

Because the local winter rain has a high *d*-excess value, the drip water and fluid inclusion data lie above the global meteoric water line (GMWL; $\delta D = 8\ \delta^{18}O + 10$) (Fig. 11). The isotope data for modern stalagmite inclusion water samples did not differ significantly from those of rain water (Section 3.1.6) and plotted within the annual rainwater variability (Fig. 11). Isotopic data for the stalagmite samples GYK2-L1 and L2 from the Early Holocene and GYK2-L3 and L6 from the LGM are depicted for the winter LMWL with high *d*-excess values (Fig. 11). Note that further evaluation of the accuracy of both $\delta^{18}O$ and δD (Section 3.1.6) is required for interpretation of the absolute value of *d*-excess. We speculate that the systematic offset from the modern values would be caused by a changes in winter/summer rainfall amount ratio.

3.2.4. Evaluation of modern $\delta^{18}O$ thermometers

Schwarcz et al. (1976) first proposed that the speleothem formation temperature could be determined from oxygen

isotope fractionation factor between the inclusion water and the coeval enclosing carbonate under equilibrium. The widely accepted fractionation factor is based on inorganic precipitation experiments (Kim and O'Neil, 1997; Kim et al., 2007). Coplen (2007) provided an equation based on single data point from Devil's Hole. Recent observations of drip water and calcite provided an empirical relationships (e.g., Demeny et al., 2010; Tremaine et al., 2011; Fairchild and Baker, 2012) (Fig. 12).

The $\delta^{18}O$ data from the farmed active calcite and drip water samples were used to evaluate the modern oxygen isotope fractionation behavior in Gyokusen Cave. The averaged $\delta^{18}O$ of the calcite precipitated on glass plates was $-5.50 \pm 0.38‰$. The equation of Coplen (2007) provides an temperature value of 22.4 ± 2.2 °C, which matches the observed value of 23.4 ± 0.5 °C (Fig. 12). The other equations by Kim et al. (2007) and Tremaine et al. (2011) provide lower temperatures of 20.3 ± 2.3 °C and 15.6 ± 2.0 °C, respectively. The limited in-situ experiment data show that the isotope fractionation behavior in Gyokusen Cave follows (1) the equation proposed by Coplen (2007), or (2) the empirical relationship given by Tremaine et al. (2011) with an additional ~0.5‰ kinetic effect. Future estimates of the fractionation factor should employ larger numbers of farmed samples because the kinetic effects vary locally (Mickler et al., 2004).

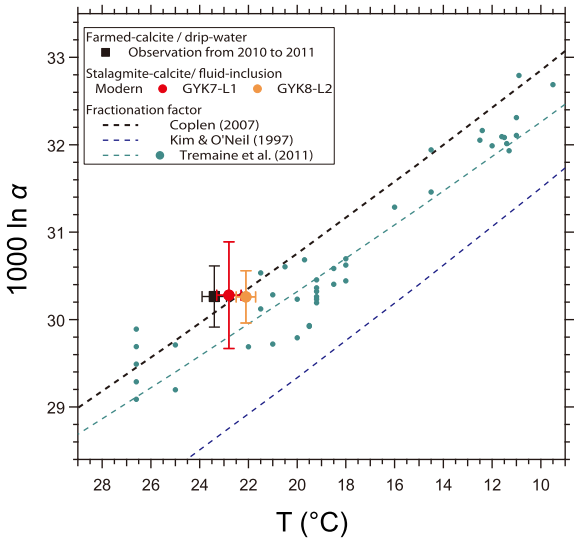

Fig. 12. 1000 ln α vs. temperature plot. The black square represents the calcite–water oxygen isotope fractionation factor of the farmed calcite at present-day cave temperature at this study site. Circles indicate the calcite vs. fluid-inclusion fractionation factor for modern stalagmites against the observed temperature during their growth periods, GYK7-L1 (red) and GYK8-L2 (orange circle). The dashed black line is the fractionation factor calibrated at the Devils Hole observation (Coplen, 2007). The green circle represents the fractionation factors observed at various caves with the best fit curve (green dashed line) (Tremaine et al., 2011). The blue dashed line is the fractionation factor based on laboratory experiment (Kim and O'Neil, 1997). (For interpretation of the references to color in this figure legend, the reader is referred to the web version of this article.)

Past isotopic fractionation behavior in the cave can be evaluated using the decades-old stalagmite data for GYK7-L1 and GYK8-L2. The calculated 1000 ln α values based on calcite and fluid inclusion measurements were $30.28 \pm 0.61‰$ for GYK7-L1, which formed in 1971–2009, and $30.26 \pm 0.30‰$ for GYK8-L2, which had a deposition interval of 1934–1970. Meteorological data at the Naha station indicate annual temperature averages of 22.9 ± 0.5 °C and 22.2 ± 0.4 °C for the GYK7-L1 and GYK8-L2 formation periods, respectively. These data points overlap with the farmed calcite, suggesting that no significant temporal changes in the isotopic fractionations occurred in previous decades (Fig. 12).

3.2.5. Paleotemperature reconstruction for the early Holocene and last glacial period

The temperature-dependent equation for calcite–water isotope fractionation in caves has been debated (Dietzel et al., 2009; Mühlinghuas et al., 2009; Demeny et al., 2010; Day and Henderson, 2011). Different equations have been applied for different caves (Affek et al., 2008; Griffiths et al., 2010; Labuhn et al., 2015). Fortunately, the temperature offset between past and modern times (ΔT) can be determined using a slope of 1000 ln α/T. For temperatures between 15 and 25 °C, the slopes range from −0.19 to −0.21‰/°C (Fig. 12). The ΔT uncertainty caused by different slopes is only ±0.4 °C between modern and the last glacial period.

The ΔT calculated using Coplen's equation versus age is depicted in Fig. 10d. The Early Holocene (9–10 ka) cave temperature values for GYK2-L1 and L2 are 3.4 ± 0.7 °C lower than the average temperatures for the two modern layers GYK7-L1 and GYK8-L2. Different fractionation factors of Kim and O'Neil (1997) and Tremaine et al. (2011) provided indistinguishable ΔT values of -3.2 ± 0.4 °C and -3.7 ± 0.7 °C, respectively.

For the last glacial period, the inferred cave temperature data from four subsamples of GYK2-L3–6 exhibit an apparently large variability of 4 °C, attributed to the kinetic fractionation in the two layers GYK2-L4 and L5 (Fig. 9, Section 3.2.1). After excluding the two biased ΔT values, the average ΔT value for GYK2-L3 and GYK2-L6 was -8.2 ± 2.4 °C (Fig. 10d).

Marine sediment proxy records indicated a sea surface temperature (SST) of 0.5–1 °C colder conditions during the Early Holocene relative to modern conditions (Jian et al., 2000; Lin et al., 2006; Yu et al., 2008). For the glacial period, the SST in the East China Sea at 26 ka are 3–4 °C lower than those estimated for the late Holocene (Xu and Oda, 1999; Ijiri et al., 2005; Yu et al., 2009). The fluid inclusions-based terrestrial temperature estimations for the two periods of 9–10 and 26 ka are 2–3 and 3–5 °C lower, respectively, than the corresponding SSTs. However, an ocean sediment core from the East China Sea showed that asynchronous marine and terrestrial changes (Xu et al., 2013). It suggests that the cave-derived temperature data could not be simply compared with marine record.

4. CONCLUSIONS

A precise and accurate procedure for measuring the $\delta^{18}O$ and δD values of stalagmite inclusion water was developed after carefully addressing several issues, including water/carbonate adsorption, spectral interference, and sample extraction. This method is reproducible and only requires 50–260 nL of inclusion water from 77 to 286 mg of stalagmite carbonate samples from Gyokusen Cave. The agreement between the isotope ratios of the inclusion water from modern stalagmites and of local rain water indicates the robustness of our developed techniques. Oxygen and hydrogen isotope data for stalagmite inclusion water suggest possible prevailing winter monsoon conditions at 26 ka. The inferred temperatures suggest 3.4 ± 0.7 °C and 8.2 ± 2.4 °C colder conditions relative to modern at 9–10 and 26 ka, respectively.

ACKNOWLEDGMENTS

We thank Sohei Ooka (Nanto Co. Ltd.), Kentaro Tanaka, Kensaku Nakamura, and Kanako Omine (University of the Ryukyus) for assistance with field surveys and laboratory work. We also thank Gregor Hsiao (Picarro Inc.) and Yuichiro Ueno (Tokyo Institute of Technology) for their comments and suggestions. This research was supported by Japan Society for the Promotion of Science (JSPS) KAKENHI Grant Number (24681005, 22840035, and 15H01729). This study was partly supported by the International Research Hub Project for Climate Change and Coral Reef Island Dynamics (University of the Ryukyus) and by JSPS KAKENHI (26707028). We also acknowledge the financial supports provided by Taiwan ROC MOST (102-2116-M-002-016, 103-2119-M-002-022, and 104-2119-M-002-003) and National Taiwan University (101R7625).

REFERENCES

Affek H. P., Bar-Matthews M., Ayalon A., Matthews A. and Eiler J. M. (2008) Glacial/interglacial temperature variations in Soreq cave speleothems as recorded by 'clumped isotope' thermometry. *Geochim. Cosmochim. Acta* **72**, 5351–5360.

Affolter S., Fleitmann D. and Leuenberger M. (2014) New online method for water isotope analysis of speleothem fluid inclusions using laser absorption spectroscopy (WS-CRDS). *Clim. Past* **10**, 1291–1304.

Arienzo M. M., Swart P. K. and Vonhof H. B. (2013) Measurement of $\delta^{18}O$ and $\delta^{2}H$ values of fluid inclusion water in speleothems using cavity ring-down spectroscopy compared with isotope ratio mass spectrometry. *Rapid Commun. Mass Spectrom.* **27**, 2616–2624.

Ayliffe L. K., Gagan M. K., Zhao J. X., Drysdale R. N., Hellstrom J. C., Hantoro W. S., Griffiths M. L., Scott-Gagan H., St Pierre E., Cowley J. A. and Suwargadi B. W. (2013) Rapid interhemispheric climate links via the Australasian monsoon during the last deglaciation. *Nat. Commun.* **4**, 2908.

Bar-Matthews M., Ayalon A., Gilmour M., Matthews A. and Hawkesworth C. J. (2003) Sea-land oxygen isotopic relationships from planktonic foraminifera and speleothems in the Eastern Mediterranean region and their implication for paleorainfall during interglacial intervals. *Geochim. Cosmochim. Acta* **67**, 3181–3199.

Bintanja R. and van de Wal R. S. W. (2008) North American ice-sheet dynamics and the onset of 100,000-year glacial cycles. *Nature* **454**, 869–872.

Blyth A. J., Baker A., Collins M. J., Penkman K. E. H., Gilmour M. A., Moss J. S., Genty D. and Drysdale R. N. (2008) Molecular organic matter in speleothems and its potential as an environmental proxy. *Quat. Sci. Rev.* **27**, 905–921.

Brand W. A., Geilmann H., Crosson E. R. and Rella C. W. (2009) Cavity ring-down spectroscopy versus high-temperature conversion isotope ratio mass spectrometry; a case study on $\delta^{2}H$ and $\delta^{18}O$ of pure water samples and alcohol/water mixtures. *Rapid Commun. Mass Spectrom.* **23**, 1879–1884.

Cheng H., Sinha A., Wang X. F., Cruz F. W. and Edwards R. L. (2012) The global paleomonsoon as seen through speleothem records from Asia and the Americas. *Clim. Dyn.* **39**, 1045–1062.

Cheng H., Edwards R. L., Shen C.-C., Polyak V. J., Asmerom Y., Woodhead J., Hellstrom J., Wang Y. J., Kong X. G., Spotl C., Wang X. F. and Alexander E. C. (2013) Improvements in ^{230}Th dating, ^{230}Th and ^{234}U half-life values, and U–Th isotopic measurements by multi-collector inductively coupled plasma mass spectrometry. *Earth Planet. Sci. Lett.* **371**, 82–91.

Coplen T. B. (2007) Calibration of the calcite–water oxygen-isotope geothermometer at Devils Hole, Nevada, a natural laboratory. *Geochim. Cosmochim. Acta* **71**, 3948–3957.

Czuppon G., Ramsay R. R., Ozgenc I., Demeny A., Gwalani L. G., Rogers K., Eves A., Papp L., Palcsu L., Berkesi M. and Downes P. J. (2014) Stable (H, O, C) and noble-gas (He and Ar) isotopic compositions from calcite and fluorite in the Speewah Dome, Kimberley Region, Western Australia: implications for the conditions of crystallization and evidence for the influence of crustal-mantle fluid mixing. *Mineral. Petrol.* **108**, 759–775.

Day C. C. and Henderson G. M. (2011) Oxygen isotopes in calcite grown under cave-analogue conditions. *Geochim. Cosmochim. Acta* **75**, 3956–3972.

Demeny A. and Siklosy Z. (2008) Combination of off-line preparation and continuous flow mass spectrometry: D/H analyses of inclusion waters. *Rapid Commun. Mass Spectrom.* **22**, 1329–1334.

Demeny A., Kele S. and Siklosy Z. (2010) Empirical equations for the temperature dependence of calcite–water oxygen isotope fractionation from 10 to 70 degrees C. *Rapid Commun. Mass Spectrom.* **24**, 3521–3526.

Dennis P. F., Rowe P. J. and Atkinson T. C. (2001) The recovery and isotopic measurement of water from fluid inclusions in speleothems. *Geochim. Cosmochim. Acta* **65**, 871–884.

Dietzel M., Tang J., Leis A. and Köhler S. J. (2009) Oxygen isotopic fractionation during inorganic calcite precipitation – effects of temperature, precipitation rate and pH. *Chem. Geol.* **268**, 107–115.

Dorale J. A., Edwards R. L., Ito E. and Gonzalez L. A. (1998) Climate and vegetation history of the midcontinent from 75 to 25 ka: a speleothem record from Crevice Cave, Missouri, USA. *Science* **282**, 1871–1874.

Dublyansky Y. V. and Spotl C. (2009) Hydrogen and oxygen isotopes of water from inclusions in minerals: design of a new crushing system and on-line continuous-flow isotope ratio mass spectrometric analysis. *Rapid Commun. Mass Spectrom.* **23**, 2605–2613.

Fairchild I. J. and Baker A. (2012) *Speleothem Science: From Process to Past Environments*, 1st ed. Wiley-Blackwell, West Sussex, UK.

Fairchild I. J., Smith C. L., Baker A., Fuller L., Spotl C., Mattey D., McDermott F. and Eimp (2006) Modification and preservation of environmental signals in speleothems. *Earth-Sci. Rev.* **75**, 105–153.

Fleitmann D., Burns S. J., Neff U., Mangini A. and Matter A. (2003) Changing moisture sources over the last 330,000 years in Northern Oman from fluid-inclusion evidence in speleothems. *Quat. Res.* **60**, 223–232.

Gascoyne M. (1992) Paleoclimate determination from cave calcite deposits. *Quat. Sci. Rev.* **11**, 609–632.

Genty D., Plagnes V., Causse C., Cattani O., Stievenard M., Falourd S., Blamart D., Ouahdi R. and Van-Exter S. (2002) Fossil water in large stalagmite voids as a tool for paleoprecipitation stable isotope composition reconstitution and paleotemperature calculation. *Chem. Geol.* **184**, 83–95.

Goede A., Green D. C. and Harmon R. S. (1986) Late Pleistocene palaeotemperature record from a Tasmanian speleothem. *Aust. J. Earth Sci.* **33**, 333–342.

Griffiths M. L., Drysdale R. N., Vonhof H. B., Gagan M. K., Zhao J. X., Ayliffe L. K., Hantoro W. S., Hellstrom J. C., Cartwright I., Frisia S. and Suwargadi B. W. (2010) Younger Dryas–Holocene temperature and rainfall history of southern Indonesia from $\delta^{18}O$ in speleothem calcite and fluid inclusions. *Earth Planet. Sci. Lett.* **295**, 30–36.

Griffiths M. L., Drysdale R. N., Gagan M. K., Hellstrom J. C., Couchoud I., Ayliffe L. K., Vonhof H. B. and Hantoro W. S. (2013) Australasian monsoon response to Dansgaard–Oeschger event 21 and teleconnections to higher latitudes. *Earth Planet. Sci. Lett.* **369**, 294–304.

Gröning M. (2011) Improved water delta H-2 and delta O-18 calibration and calculation of measurement uncertainty using a simple software tool. *Rapid Commun. Mass Spectrom.* **25**, 2711–2720.

Gupta P., Noone D., Galewsky J., Sweeney C. and Vaughn B. H. (2009) Demonstration of high-precision continuous measurements of water vapor isotopologues in laboratory and remote field deployments using wavelength-scanned cavity ring-down spectroscopy (WS-CRDS) technology. *Rapid Commun. Mass Spectrom.* **23**, 2534–2542.

Harmon R. S., Schwarcz H. P. and O'Neil J. R. (1979) D/H ratios in speleothem fluid inclusions: a guide to variations in the isotopic composition of meteoric precipitation? *Earth Planet. Sci. Lett.* **42**, 254–266.

Hendy C. H. (1971) The isotope geochemistry of speleothems-I. The calculation of the effects of different modes of formation on the isotopic composition of speleothems and their applicability. *Geochim. Cosmochim. Acta* **35**, 801–824.

Hiess J., Condon D. J., McLean N. and Noble S. R. (2012) $^{238}U/^{235}U$ systematics in terrestrial uranium-bearing minerals. *Science* **335**, 1610–1614.

Ijiri A., Wang L. J., Oba T., Kawahata H., Huang C. Y. and Huang C. Y. (2005) Paleoenvironmental changes in the northern area of the East China Sea during the past 42,000 years. *Palaeogeogr. Palaeoclimatol.* **219**, 239–261.

Jaffey A. H., Flynn K. F., Glendenin L. E., Bentley W. C. and Essling A. M. (1971) Precision measurement of half-lives and specific activities of ^{235}U and ^{238}U. *Phys. Rev. C* **4**, 1889–1906.

Jasechko S., Lechler A., Pausata F. S. R., Fawcett P. J., Gleeson T., Cendón D. I., Galewsky J., LeGrande A. N., Risi C., Sharp Z. D., Welker J. M., Werner M. and Yoshimura K. (2015) Glacial–interglacial shifts in global and regional precipitation $\delta^{18}O$. *Clim. Past Discuss.* **11**, 831–872.

Jian Z. M., Wang P. X., Saito Y., Wang J. L., Pflaumann U., Oba T. and Cheng X. R. (2000) Holocene variability of the Kuroshio Current in the Okinawa Trough, northwestern Pacific Ocean. *Earth Planet. Sci. Lett.* **184**, 305–319.

Kim S. T. and O'Neil J. R. (1997) Equilibrium and nonequilibrium oxygen isotope effects in synthetic carbonates. *Geochim. Cosmochim. Acta* **61**, 3461–3475.

Kim S. T., Mucci A. and Taylor B. E. (2007) Phosphoric acid fractionation factors for calcite and aragonite between 25 and 75 degrees C: revisited. *Chem. Geol.* **246**, 135–146.

Labuhn I., Genty D., Vonhof H., Bourdin C., Blamart D., Douville E., Ruan J., Cheng H., Edwards R. L., Pons-Branchu E. and Pierre M. (2015) A high-resolution fluid inclusion $\delta^{18}O$ record from a stalagmite in SW France: modern calibration and comparison with multiple proxies. *Quat. Sci. Rev.* **110**, 152–165.

Lachniet M. S. (2009) Climatic and environmental controls on speleothem oxygen-isotope values. *Quat. Sci. Rev.* **28**, 412–432.

Lauritzen S. E. and Lundberg J. (1999) Calibration of the speleothem delta function: an absolute temperature record for the Holocene in northern Norway. *Holocene* **9**, 659–669.

Lin Y.-S., Wei K.-Y., Lin I.-T., Yu P.-S., Chiang H.-W., Chen C.-Y., Shen C.-C., Mii H.-S. and Chen Y.-G. (2006) The Holocene *Pulleniatina* Minimum Event revisited: geochemical and faunal evidence from the Okinawa Trough and upper reaches of the Kuroshio current. *Mar. Micropaleontol.* **59**, 153–170.

Liu Z. Y., Wen X. Y., Brady E. C., Otto-Bliesner B., Yu G., Lu H. Y., Cheng H., Wang Y. J., Zheng W. P., Ding Y. H., Edwards R. L., Cheng J., Liu W. and Yang H. (2014) Chinese cave records and the East Asia Summer Monsoon. *Quat. Sci. Rev.* **83**, 115–128.

Mangini A., Spotl C. and Verdes P. (2005) Reconstruction of temperature in the Central Alps during the past 2000 yr from a delta O-18 stalagmite record. *Earth Planet. Sci. Lett.* **235**, 741–751.

Matthews A., Ayalon A. and Bar-Matthews M. (2000) D/H ratios of fluid inclusions of Soreq cave (Israel) speleothems as a guide to the Eastern Mediterranean Meteoric Line relationships in the last 120 ky. *Chem. Geol.* **166**, 183–191.

McDermott F. (2004) Palaeo-climate reconstruction from stable isotope variations in speleothems: a review. *Quat. Sci. Rev.* **23**, 901–918.

McDermott F., Schwarcz H. and Rowe P. J. (2005) Isotopes in speleothems. In *Isotopes in Palaeoenvironmental Research* (ed. M. J. Leng). Springer, Dordrecht, pp. 185–226.

McGarry S. F. and Baker A. (2000) Organic acid fluorescence: applications to speleothem palaeoenvironmental reconstruction. *Quat. Sci. Rev.* **19**, 1087–1101.

McGarry S., Bar-Matthews M., Matthews A., Vaks A., Schilman B. and Ayalon A. (2004) Constraints on hydrological and paleotemperature variations in the Eastern Mediterranean region in the last 140 ka given by the δD values of speleothem fluid inclusions. *Quat. Sci. Rev.* **23**, 919–934.

Merlivat L. and Jouzel J. (1979) Global climatic interpretation of the deuterium-oxygen 18 relationship for precipitation. *J. Geophys. Res.* **84**, 5029–5033.

Mickler P. J., Banner J. L., Stern L., Asmerom Y., Edwards R. L. and Ito E. (2004) Stable isotope variations in modern tropical speleothems: evaluating equilibrium vs. kinetic isotope effects. *Geochim. Cosmochim. Acta* **68**, 4381–4393.

Mühlinghuas C., Scholz D. and Mangini A. (2009) Modelling fractionation of stable isotopes in stalagmites. *Geochim. Cosmochim. Acta* **73**, 7275–7289.

Olsen J., Seierstad I., Vinther B., Johnsen S. and Heinemeier J. (2006) Memory effect in deuterium analysis by continuous flow isotope ratio measurement. *Int. J. Mass Spectrom.* **254**, 44–52.

Partin J. W., Cobb K. M., Adkins J. F., Clark B. and Fernandez D. P. (2007) Millennial-scale trends in west Pacific warm pool hydrology since the Last Glacial Maximum. *Nature* **449**, 452–455.

Schultz N. M., Griffis T. J., Lee X. H. and Baker J. M. (2011) Identification and correction of spectral contamination in $^{2}H/^{1}H$ and $^{18}O/^{16}O$ measured in leaf, stem, and soil water. *Rapid Commun. Mass Spectrom.* **25**, 3360–3368.

Schwarcz H. P., Harmon R. S., Thompson P. and Ford D. C. (1976) Stable isotope studies of fluid inclusions in speleothems and their paleoclimatic significance. *Geochim. Cosmochim. Acta* **40**, 657–665.

Shen C.-C., Cheng H., Edwards R. L., Moran S. B., Edmonds H. N., Hoff J. A. and Thomas R. B. (2003) Measurement of attogram quantities of ^{231}Pa in dissolved and particulate fractions of seawater by isotope dilution thermal ionization mass spectroscopy. *Anal. Chem.* **75**, 1075–1079.

Shen C.-C., Li K.-S., Sieh K., Natawidjaja D., Cheng H., Wang X., Edwards R. L., Lam D. D., Hsieh Y.-T., Fan T.-Y., Meltzner A. J., Taylor F. W., Quinn T. M., Chiang H.-W. and Kilbourne K. H. (2008) Variation of initial ^{230}Th/^{232}Th and limits of high precision U–Th dating of shallow-water corals. *Geochim. Cosmochim. Acta* **72**, 4201–4223.

Shen C.-C., Wu C.-C., Cheng H., Edwards R. L., Hsieh Y.-T., Gallet S., Chang C.-C., Li T.-Y., Lam D. D., Kano A., Hori M. and Spotl C. (2012) High-precision and high-resolution carbonate ^{230}Th dating by MC-ICP-MS with SEM protocols. *Geochim. Cosmochim. Acta* **99**, 71–86.

Sundqvist H. S., Holmgren K., Fohlmeister J., Zhang Q., Bar Matthews M., Spotl C. and Kornich H. (2013) Evidence of a large cooling between 1690 and 1740 AD in southern Africa. *Sci. Rep. (UK)* **3**, 1767.

Talma A. S. and Vogel J. C. (1992) Late quaternary paleotemperatures derived from a speleothem from Cango Caves, Cape Province, South Africa. *Quat. Res.* **37**, 203–213.

Tatár E., Mihucz V. G., Zámbo L., Gasparics T. and Záray G. (2004) Seasonal changes of fulvic acid, Ca and Mg concentrations of water samples collected above and in the Beke Cave of the Aggtelek karst system (Hungary). *Appl. Geochem.* **19**, 1727–1733.

Tharammal T., Paul A., Merkel U. and Noone D. (2013) Influence of Last Glacial Maximum boundary conditions on the global water isotope distribution in an atmospheric general circulation model. *Clim. Past* **9**, 789–809.

Tremaine D. M., Froelich P. N. and Wang Y. (2011) Speleothem calcite farmed in situ: modern calibration of δ^{18}O and δ^{13}C paleoclimate proxies in a continuously-monitored natural cave system. *Geochim. Cosmochim. Acta* **75**, 4929–4950.

Uemura R., Matsui Y., Motoyama H. and Yoshida N. (2007) Deuterium and oxygen-18 determination of microliter quantities of a water sample using an automated equilibrator. *Rapid Commun. Mass Spectrom.* **21**, 1783–1790.

Uemura R., Matsui Y., Yoshimura K., Motoyama H. and Yoshida N. (2008) Evidence of deuterium excess in water vapor as an indicator of ocean surface conditions. *J. Geophys. Res. Atmos.* **113**. http://dx.doi.org/10.1029/2008JD010209, D19114.

Uemura R., Yonezawa N., Yoshimura K., Asami R., Kadena H., Yamadae K. and Yoshida N. (2012) Factors controlling isotopic composition of precipitation on Okinawa Island, Japan: implications for paleoclimate reconstruction in the East Asian Monsoon region. *J. Hydrol.* **475**, 314–322.

van Breukelen M. R., Vonhof H. B., Hellstrom J. C., Wester W. C. G. and Kroon D. (2008) Fossil dripwater in stalagmites reveals Holocene temperature and rainfall variation in Amazonia. *Earth Planet. Sci. Lett.* **275**, 54–60.

Verheyden S., Genty D., Cattani O. and van Breukelen M. R. (2008) Water release patterns of heated speleothem calcite and hydrogen isotope composition of fluid inclusions. *Chem. Geol.* **247**, 266–281.

Vonhof H. B., van Breukelen M. R., Postma O., Rowe P. J., Atkinson T. C. and Kroon D. (2006) A continuous-flow crushing device for on-line δ^2H analysis of fluid inclusion water in speleothems. *Rapid Commun. Mass Spectrom.* **20**, 2553–2558.

Wang Y. J., Cheng H., Edwards R. L., An Z. S., Wu J. Y., Shen C. C. and Dorale J. A. (2001) A high-resolution absolute-dated Late Pleistocene monsoon record from Hulu Cave, China. *Science* **294**, 2345–2348.

Wang X. F., Auler A. S., Edwards R. L., Cheng H., Ito E. and Solheid M. (2006) Interhemispheric anti-phasing of rainfall during the last glacial period. *Quat. Sci. Rev.* **25**, 3391–3403.

Wang Y. J., Cheng H., Edwards R. L., Kong X. G., Shao X. H., Chen S. T., Wu J. Y., Jiang X. Y., Wang X. F. and An Z. S. (2008) Millennial- and orbital-scale changes in the East Asian monsoon over the past 224,000 years. *Nature* **451**, 1090–1093.

West A. G., Goldsmith G. R., Brooks P. D. and Dawson T. E. (2010) Discrepancies between isotope ratio infrared spectroscopy and isotope ratio mass spectrometry for the stable isotope analysis of plant and soil waters. *Rapid Commun. Mass Spectrom.* **24**, 1948–1954.

Wiedner E., Scholz D., Mangini A., Polag D., Muhlinghaus C. and Segl M. (2008) Investigation of the stable isotope fractionation in speleothems with laboratory experiments. *Quat. Int.* **187**, 15–24.

Xu X. D. and Oda M. (1999) Surface-water evolution of the eastern East China Sea during the last 36,000 years. *Mar. Geol.* **156**, 285–304.

Xu D. K., Lu H. Y., Wu N. Q., Liu Z. X., Li T. G., Shen C. M. and Wang L. (2013) Asynchronous marine-terrestrial signals of the last deglacial warming in East Asia associated with low- and high-latitude climate changes. *Proc. Natl. Acad. Sci. U.S.A.* **110**, 9657–9662.

Yonge C. J. (1982) *Stable Isotope Studies of Water Extracted from Speleothems*. McMaster University.

Yu H., Xiong Y. Q., Liu Z. X., Berne S., Huang C. Y. and Jia G. D. (2008) Evidence for the 8200 a BP cooling event in the middle Okinawa Trough. *Geo-Mar. Lett.* **28**, 131–136.

Yu H., Liu Z. X., Berne S., Jia G. D., Xiong Y. Q., Dickens G. R., Wei G. J., Shi X. F., Liu J. P. and Chen F. J. (2009) Variations in temperature and salinity of the surface water above the middle Okinawa Trough during the past 37 kyr. *Palaeogeogr. Palaeoclimatol.* **281**, 154–164.

Zhang R., Schwarcz H. P., Ford D. C., Schroeder F. S. and Beddows P. A. (2008) An absolute paleotemperature record from 10 to 6 Ka inferred from fluid inclusion D/H ratios of a stalagmite from Vancouver Island, British Columbia, Canada. *Geochim. Cosmochim. Acta* **72**, 1014–1026.

Zhao L. J., Xiao H. L., Zhou J., Wang L. X., Cheng G. D., Zhou M. X., Yin L. and McCabe M. F. (2011) Detailed assessment of isotope ratio infrared spectroscopy and isotope ratio mass spectrometry for the stable isotope analysis of plant and soil waters. *Rapid Commun. Mass Spectrom.* **25**, 3071–3082.

Associate editor: Miryam Bar-Matthews